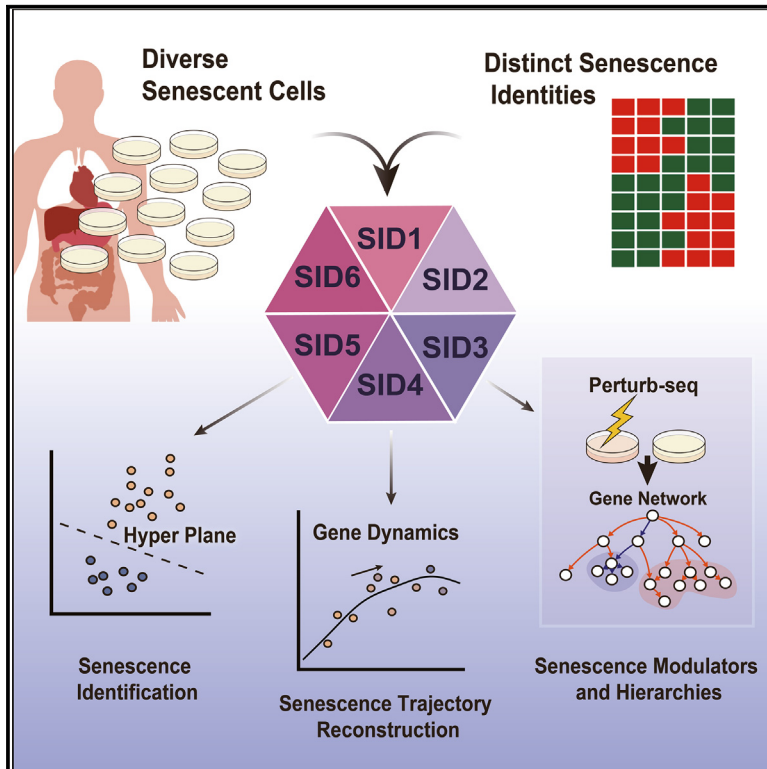


# Cell Metabolism

## Single-cell senescence identification reveals senescence heterogeneity, trajectory, and modulators

### Graphical abstract



### Authors

Wanyu Tao, Zhengqing Yu,  
Jing-Dong J. Han

### Correspondence

jackie.han@pku.edu.cn

### In brief

Tao et al. developed a computational program that identifies and tracks 6 types of senescent cells based on single-cell transcriptomes from tens of thousands of cells.

### Highlights

- The SenCID program is developed to identify senescent cells from bulk or scRNA-seq
- SenCID finds six modes of senescence among cell types with different characteristics
- SenCID finds varied trajectories in aging and disease to common senescent endpoint
- SenCID identifies genome-wide senescence modulators and their hierarchies

## Resource

# Single-cell senescence identification reveals senescence heterogeneity, trajectory, and modulators

Wanyu Tao,<sup>1</sup> Zhengqing Yu,<sup>1</sup> and Jing-Dong J. Han<sup>1,2,3,\*</sup>

<sup>1</sup>Peking-Tsinghua Center for Life Sciences, Academy for Advanced Interdisciplinary Studies, Center for Quantitative Biology (CQB), Peking University, Beijing, China

<sup>2</sup>Peking University Chengdu Academy for Advanced Interdisciplinary Biotechnologies, Chengdu, China

<sup>3</sup>Lead contact

\*Correspondence: [jackie.han@pku.edu.cn](mailto:jackie.han@pku.edu.cn)

<https://doi.org/10.1016/j.cmet.2024.03.009>

## SUMMARY

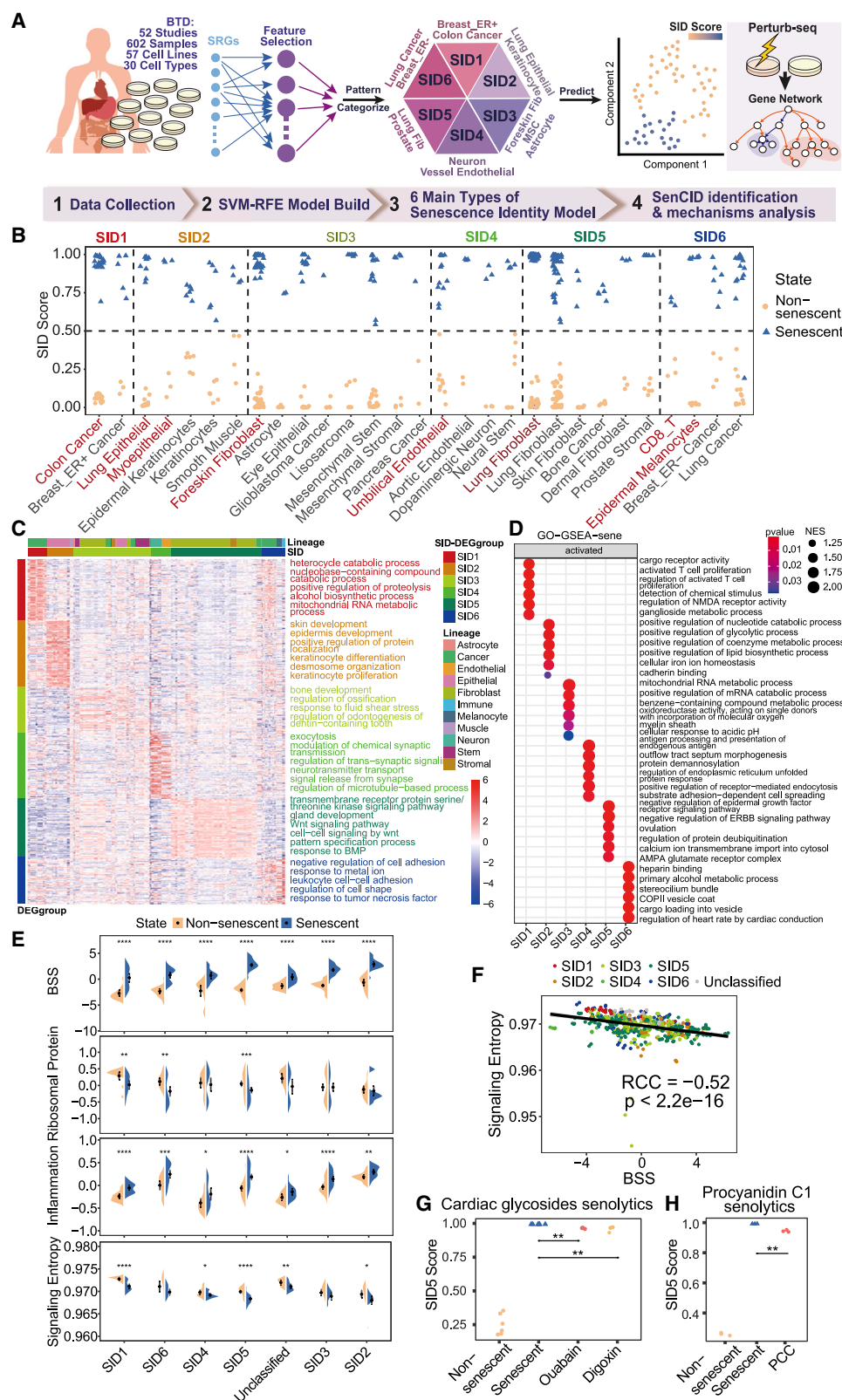
Cellular senescence underlies many aging-related pathologies, but its heterogeneity poses challenges for studying and targeting senescent cells. We present here a machine learning program senescent cell identification (SenCID), which accurately identifies senescent cells in both bulk and single-cell transcriptome. Trained on 602 samples from 52 senescence transcriptome datasets spanning 30 cell types, SenCID identifies six major senescence identities (SIDs). Different SIDs exhibit different senescence baselines, stemness, gene functions, and responses to senolytics. SenCID enables the reconstruction of senescent trajectories under normal aging, chronic diseases, and COVID-19. Additionally, when applied to single-cell Perturb-seq data, SenCID helps reveal a hierarchy of senescence modulators. Overall, SenCID is an essential tool for precise single-cell analysis of cellular senescence, enabling targeted interventions against senescent cells.

## INTRODUCTION

Cellular senescence is a state of permanent cell cycle arrest<sup>1</sup> induced by multiple types of stresses, including over-replication, DNA-damage-stress-like radiation, oxidative stress, and oncogene activation.<sup>2,3</sup> Both proliferating and post-mitotic cells (e.g., fully differentiated cells) can be induced to senescence,<sup>3,4</sup> which exhibit various senescence-related phenotypes, like increased size of nucleoli, enlarged and overloaded lysosome, and secretion of senescence-associated secretory phenotype (SASP) factors.<sup>5–7</sup> Senescent cells accumulate inside the body during aging<sup>4,8</sup> and contribute to the initiation and progression of various aging-related chronic diseases.<sup>9–11</sup> Treatments to target and kill senescent cells, like senolytics, have shown promising results in extending lifespans and ameliorating various diseases.<sup>12,13</sup> The target specificity and toxicity to non-senescent cells is still a big hurdle for clinical applications of the current senolytic treatments.<sup>14,15</sup> Wrongly targeting quiescent (a state where the cells temporarily arrest for growth but reversible<sup>6</sup>) or differentiated cells as senescent cells obviously has dire consequences. Furthermore, there are beneficial effects of senescent cells in certain circumstances, which brings more critical requirements to study the right time and condition for senolytics to overcome the harmful effects.<sup>16</sup> Besides, senescence patterns are variable across cell types, tissues, and inductions.<sup>17</sup> Some senolytic drugs are effective in some cell types but not others, suggestive of differential patterns or modes of senescence among

cells,<sup>18</sup> making it an urgent need to identify these differential patterns and their specific regulators, thus to enhance treatment efficacy and specificity.

To better target the senescent cells, it is essential to accurately identify senescent cells in different biological environments. Unfortunately, there is currently no single marker that is unique for senescent cells.<sup>19</sup> Experimentally, SA- $\beta$ -gal staining<sup>20</sup> and expression of cyclin-dependent kinase (CDK) inhibitors like p16 and p21 are commonly used to characterize senescence. While these markers identify senescent cells in most of the biological contexts, they are not universal, as some cell types express these markers at non-senescent stage.<sup>7,19,21</sup> Also, technical issues may bring inconsistency when detecting these markers. At the transcriptome level, using databases with annotated senescence-related genes (SRGs)<sup>7,22–24</sup> to estimate the level of cellular senescence by either tally the normalized value<sup>25</sup> or the ranking of these genes<sup>26</sup> provides some crude estimation of senescent versus dedifferentiated proliferating cells and has been applied mainly on tumor tissues.<sup>26,27</sup> However, these crude estimations are still limited in applications during normal aging and tissue degeneration, as quiescent or differentiated cells dominate in such cases instead of proliferating cancer cells. With the advance of single-cell transcriptome sequencing, computational tools to identify and quantify single-cell stemness become essential for delineating the differentiation tree, hierarchy, and their regulations.<sup>28–32</sup> Likewise, a robust metrics for senescence identification and quantification at single-cell level,



(legend on next page)

overcoming the high drop-out rate and heterogeneity, will facilitate reconstruction of cellular senescence trajectories and regulatory hierarchies,<sup>33,34</sup> thus a deeper understanding of senescence.

To address these challenges, we develop a machine learning-based program senescent cell identification (SenCID) trained on a compendium of 52 senescence transcriptome datasets of 602 samples, 30 cell types. SenCID reveals 6 major senescence identities (SIDs) for different cell types that have overlapping but differential functional biases and sensitivity to certain senolytics. SenCID performs well on both bulk and single-cell RNA sequencing data and enables reconstruction of single-cell senescence trajectories in normal aging and disease conditions, as well as mapping genome-wide senescence modulating landscape based on single-cell perturbation screens.

## RESULTS

### Heterogeneity of senescence signatures across cell types

To develop a program applicable to a broad range of cellular senescence identification, we collect published transcriptome data from 602 samples across 52 senescence-related studies, including 306 senescent and 296 non-senescent labels.<sup>17,21,27,35–80</sup> The bulk transcriptome dataset (BTD) contain 57 types of cell lines and 30 cell types with various senescence inductions (Figures S1A and S1B; Table S1). We first compare 3 different machine learning methods, supporting vector machine (SVM), random forest, and deep-neural-network-based multi-layer perceptron classifier (MLPC), along with a routine gene set ranking method (gene set variation analysis, GSVA),<sup>26</sup> based on a gene set with 1,290 SRGs collected from literature (STAR Methods). We implement a leave-one-cell-type-out strategy for all the machine learning methods (STAR Methods) and use areas under receiver operator characteristic (ROC) curves (AUCs) from predictions on each test set. The machine learning algorithms generally perform better (with ROC AUCs over 0.9 in 88.9% of cell types in average) than GSVA (with AUC over 0.9 in 76.6% of cell types) (Figure S1C). Furthermore, when only considering the ability to distinguish senescent cells from quiescent cells, machine learning methods (with AUC over 0.9 in 80% of cell types in average) perform much better than GSVA (with AUC over 0.9 in only 20% of cell types) (Figure S1D), suggesting that the machine learning models are more specific to the senescence state, making

them applicable to normal aging and degenerative processes, rather than being limited to cancers and proliferating cell lines.

Among the three machine learning methods we tested, SVM performs the best, with AUC over 0.9 in 96.7% of cell types (Figure S1C). Therefore, we use SVM to develop the SenCID program and define a basal senescent score (BSS) for each sample based on its decision values from SVM, representing the senescence-related gene expression level. We find that BSS does not vary across different cell lines or after different senescence-inducing methods for one cell type (Figures S1E and S1F) but varies across different cell types and increases after senescence induction (Figure S1G). Some cell types, like vascular smooth muscle cells, have high BSS even without senescence induction (average of 0.88), while others, like dopaminergic neuron cells, have low absolute BSS even after senescence induction (average of  $-1.28$ ), making it difficult to use a uniform standard to identify senescence in different cell types.

### 6 SID models to characterize senescence of different cell types

To determine the senescence signatures of different cell types, we employ the recursive feature elimination (RFE) method<sup>81</sup> to eliminate the unimportant feature genes from the initial 1,290 SRGs (Figures 1A and S2A, STAR Methods). We conduct the training of the RFE-SVM model independently for each distinct cell type. If a model trained on a specific cell type demonstrates accuracies over 0.95 on other cell types, these other cell types are categorized into the same senescent identity (SID) group, and the respective model is regarded as one SID model. As a result, we identify 6 such SIDs that cover 28 of the 30 cell types. Logistic regression is then used to normalize each SID model's senescence scores to be within the range of 0 to 1 (Figures S2A and S2B, STAR Methods), with each SID model correctly separating all senescent and non-senescent cells using the same threshold of SID score 0.5 (Figure 1B), except a few samples that were reported abnormal by the original publication.<sup>27</sup> The remaining two cancer cell types (liver cancer and melanoma cells) can be partly but not fully characterized by SID1 and SID6 models, respectively (Figures S2C and S2D).

### Different SIDs have overlapping but differential gene functions and different response to senolytics

The RFE-selected feature numbers are different among SIDs (Figure S2E). Notably, we find that none of the RFE-selected

**Figure 1. Identification of six distinct senescence-associated SID types by SenCID**

- (A) Schematic diagram of the SenCID model construction and its application to bulk and single-cell transcriptomes.  
(B) Performance evaluation of each SID model on its respective cell types. For the training data (red-label), SID scores are obtained from 5-fold cross-validation, while for independent validation data (black-label), SID scores are predicted by SenCID.  
(C) Heatmap showing normalized expression values of highly expressed differentially expressed genes (DEGs) (rows) among non-senescent samples (columns) in all six SIDs. The top enriched gene functions on Gene Ontology (GO)-term are annotated on the right.  
(D) Representative GSEA GO terms enriched by senescent-versus-non-senescent DEGs unique in each SID.  
(E) Distribution of basal senescence scores (BSS), ribosomal proteins, inflammation, and signaling entropy of all BTD samples in each SID, calculated by GSVA. Central dot and error bars represent the mean value and the 95% confidence interval. Significance between senescent versus non-senescent samples is marked above (\* $p < 0.05$ ; \*\* $p < 0.01$ ; \*\*\* $p < 0.001$ ; \*\*\*\* $p < 0.0001$ ; two-tailed Student's  $t$  test).  
(F) Negative correlation (Spearman correlation  $RCC = -0.52$ ,  $p < 2.2 \times 10^{-16}$ ) between signaling entropy and BSS across different cell types, colored by SID types.  
(G) Reduction of SID5 scores upon senolytic treatments with cardiac glycosides (Ouabain 50 nM, digoxin 100 nM, treated for 36 h) on lung fibroblasts (\*\* $p < 0.01$ , two-tailed Student's  $t$  test).  
(H) Reduction of SID5 scores upon senolytic treatments with procyanidin C1 (PCC, 50  $\mu$ M) on prostate stromal cells (\*\* $p < 0.01$ , two-tailed Student's  $t$  test).  
See also Figures S1–S3.



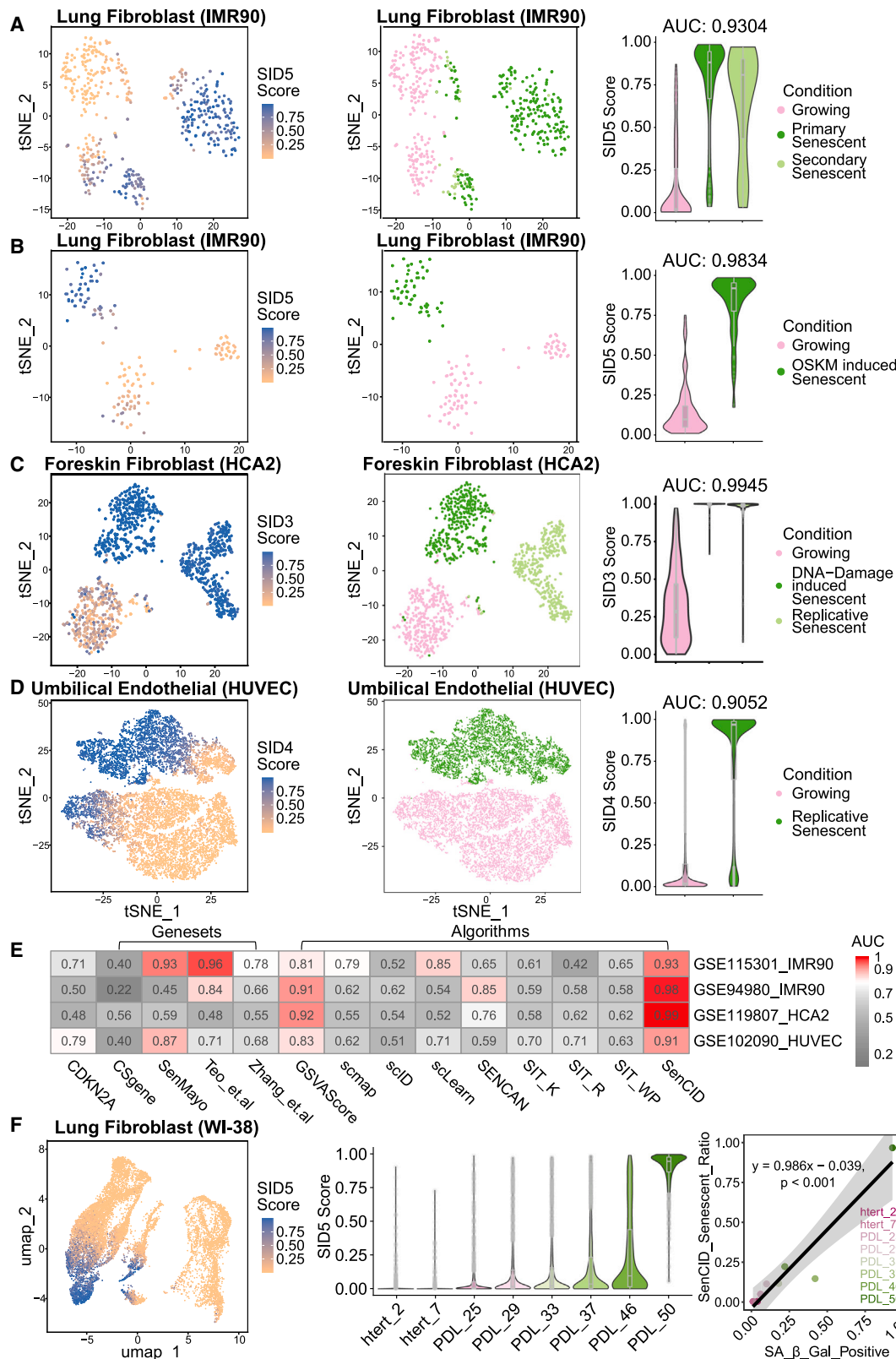


**Figure 2. Performance evaluation of SenCID on single cells**

(A–D) tSNE embedding of different cell lines based on high variable genes, colored by SID scores (left) and senescence-induction treatments (middle), and the violin plot of SID scores under different treatments (right).

(legend continued on next page)

feature genes are shared by all six SID models, even for some well-known senescence indicators (such as CDKN2A, the p16-encoding gene, and CDKN1A, the p21-encoding gene), indicating that there is no single common determinant marker of senescence (Figure S2F). Interestingly, the SID grouping did not fully overlap with tissue types, although there is partial overlap with cell lineages represented by their cellular functions (Figure 1C; Table S2), e.g., the genes highly expressed in SID2 are related to epidermal development. We also construct an SVM multi-classifier trained by BTD to automatically determine which SID a cell belongs to, with a high accuracy of 0.998 by 10-fold cross-validation (Figures S2A and S2G).

The canonical senescence signatures, including lysosome, secretome transportation, and inflammatory response, are commonly enriched in the differentially expressed genes (DEGs) of senescent versus non-senescent cells in different SID groups (Figures S3A and S3B). However, most gene functions are specifically enriched in a single SID (Figures 1D and S3A; Table S3), indicating that different SIDs may represent different aspects of senescence. For example, SID2 shows enrichment for lipids and nucleotides synthesis, SID3 for mitochondria and redox reactions, and SID4 for unfolded protein response. As expected, cell cycle checkpoint-related genes are generally downregulated with senescence, except for G1/S checkpoint genes in SID4 and SID6, where they are expressed at low levels in both senescent and non-senescent samples (Figures S3C and S3E).

Senescent cells typically experience inactivated ribosomal biogenesis due to the loss of proliferation and normal cell functions. However, the over-secretion of SASPs consumes excessive ribosomes.<sup>82</sup> We find a significant downregulation of overall ribosomal protein levels in SID1, 5, and 6 upon senescence, whereas there is no significant change in other SIDs (Figure 1E). Intriguingly, cell differentiation potency, as measured by signaling entropy, is significantly downregulated upon senescence in SID1, 2, 4, and 5 (Figure 1E), whereas inflammation scores show the opposite trend (Figure 1E). There is a significant negative correlation between signaling entropy and ribosome expression levels with BSS (Spearman correlation  $-0.52$  and  $-0.26$ , respectively,  $p < 2.2 \times 10^{-16}$ , Figures 1F and S3F), indicating that senescence heterogeneity exists across different cell types and that cell types with higher pluripotency and ribosome levels exhibit lower “senescence baselines.”

Senolytic treatments targeting anti-apoptotic members of the BCL2 family have shown promise in selectively eliminating senescent cells.<sup>18,83,84</sup> Our analysis finds that anti-apoptotic BCL2 family genes are most significantly upregulated in SID5 cells upon senescence (Figure S3G), indicating a potential for more specific targeting of senescent cells in SID5 with BCL2 inhibitors. We also find that lung fibroblasts and prostate stromal cells, commonly used as models for senolytic drug development, are classified as SID5 by SenCID (Figure S3H) in two inde-

pendent datasets<sup>85</sup> and show significantly reduced scores after various senolytic treatments (Figures 1G and 1H). SID5 scores after senolytic treatments do not drop back to the non-senescence level, similar to the SA- $\beta$ -gal staining results in the original study under the same drug concentration.<sup>86</sup> Overall, our analysis also reveals the heterogeneity of senescence response to different treatments across the different SIDs.

### SenCID distinguishes senescence from other resembling cellular states

Besides quiescence, there are some other cellular states that resemble senescence in certain aspects. For example, activated fibroblasts are known to express many pro-inflammatory factors,<sup>87</sup> and macrophages generally express p16.<sup>88,89</sup> To validate SenCID's specificity, we tested whether SenCID would give false positive predictions under such conditions. Multiple datasets were employed to test SenCID's responsiveness to various fibroblast activations, such as eosinophil-degranulation products,<sup>87</sup> transforming growth factor  $\beta$  (TGF- $\beta$ ) treatment,<sup>90</sup> and cancer cell co-culture.<sup>91</sup> SID scores remained stably low across these conditions (Figures S4A–S4C). Similarly, SenCID predicted low senescence levels in macrophages<sup>92</sup> and induced pluripotent stem cell (iPSC)-derived T cells,<sup>93</sup> despite slight score elevations post-T cell activation (Figures S4D and S4E). Furthermore, although persistent DNA damage response is widely accepted as the origin of senescence,<sup>2</sup> it should not be confused with acute genotoxic response and short-term DNA repair that finally recover the cells. We show in a time-series dataset that SID scores hardly change at 2 h right after low- or high-dose of bleomycin treatments, when almost all cells had DNA damage foci in both groups.<sup>45</sup> Moreover, the SID scores of low-dose bleomycin treated cells are still comparable to the control group within days after the treatment, while the high-dose group get into senescence, revealing that SenCID does not take the acute response or successful repair process as senescence (Figure S4F). Similarly, the SID scores hardly change in TK6 cells 4 h after treatments with different genotoxic compounds (Figure S4G), when their clastogen or aneugenic biomarkers ( $\gamma$ -H2AX, p-H3, etc.) are significantly increased.<sup>94</sup> Overall, SenCID accurately identifies senescence distinguishing it from other cellular states partially resembling senescence.

### SenCID for single cells

We evaluate the performance of the SID models on single-cell data of three cell types, which correspond to SID3, SID4, and SID5 in BTD.<sup>44,53,95,96</sup> To correct for drop-out reads, we use deep count autoencoder (DCA)<sup>97</sup> for imputation. SenCID gave the same SID classification on the single-cell data as on the respective BTD for each cell type (Figures S4H and 1B) and effectively distinguished cells with and without senescence induction, with AUCs over 0.9 (Figures 2A–2D). We conducted a comprehensive comparison with alternative methodologies,<sup>24,26,27,95,98–103</sup>

(E) Benchmarking SenCID against single canonical marker (CDKN2A), senescent gene module scores, and various cell annotators in classifying senescent cells in single-cell senescence datasets.

(F) UMAP embedding colored by SID scores (left), the violin plot of the SID scores with increasing number of passages (PDL) or with immortalization (htert) (middle), and linear regression ( $p < 0.001$ ) of senescence ratios (determined by binarization threshold of 0.5) with the corresponding SA- $\beta$ -gal staining positive ratios (right). AUC on top of the violin plots denotes the area under the ROC-curves for the SID model to discriminate the senescent versus non-senescent cells. See also Figure S4.

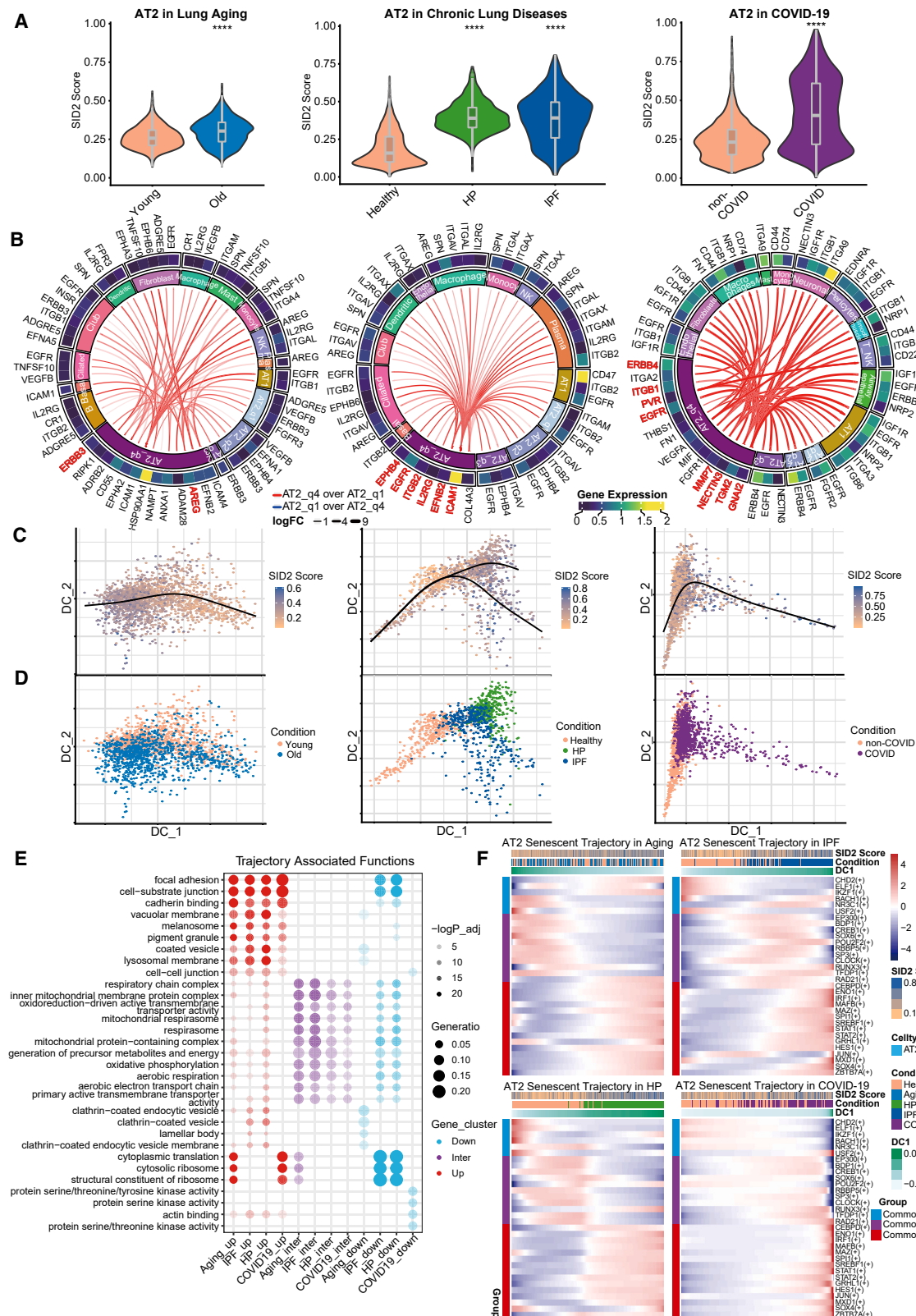


**Figure 3. Quantification and trajectories of single-cell senescence in human lung aging and diseases**

(A) Distribution of SID2 scores in AT2 cells of lungs in aged humans (left), humans with chronic diseases (IPF and HP, middle), and those with COVID-19 (right), along with their respective controls. Significance of difference from respective controls is determined by Wilcoxon test (\*\*\*\*p < 0.0001).

(legend continued on next page)

such as the single canonical marker (CDKN2A), module scores of different senescence-related gene sets, and various cell annotators (Figures 2E and S4B–S4M). Notably, although the gene set of DEGs from Teo et al. demonstrates remarkable accuracy on its own data (GEO: GSE115301), the performance is poor on other datasets, especially on different cell types. Conversely, SenCID consistently emerges as the top-performing method across all datasets, showcasing its proficiency in terms of accuracy and robustness. Furthermore, on a single-cell data of lung fibroblasts covering a time course toward replicative senescence,<sup>104</sup> SID scores show a progressive increase with cell passage and reach a large spike at passage 50, consistent with the ratio of SA- $\beta$ -gal-positive cells in the original study (Figure 2F).<sup>104</sup> Our analysis reveals that the BT-D-trained SenCID is applicable to both Drop-seq- (Figures 2A, 2C, 2D, and 2F) and Smart-seq- (Figure 2B) generated single-cell data.

### SenCID reveals heterogeneous single-cell senescence trajectories during lung aging and diseases

In order to investigate the contribution of senescence to age-related and disease-related changes in human tissues, we apply SenCID to single-cell RNA sequencing data from lung samples of individuals with normal aging, chronic lung diseases such as idiopathic pulmonary fibrosis (IPF) and hypersensitivity pneumonitis (HP), and COVID-19.<sup>25,105–107</sup> As expected, SenCID classifies different cell types into different SIDs, and we find that aged or diseased lungs have significantly higher SID scores compared with their controls in most cell types, especially alveolar type II epithelial (AT2) cells in SID2 (Figures S5A–S5C and 3A). Furthermore, AT2 cells with top 25% SID2 scores (AT2\_q4) exhibit significantly higher levels of cell-cell interactions, particularly involving inflammation ligand-receptor pairs, than those with low SID2 scores (AT2\_q1) (Figure 3B; Table S4). Notably, autocrine actions account for higher proportions of the elevated interaction pairs in IPF AT2\_q4 cells (11 out of 121 pairs) and COVID-19 AT2\_q4 cells (26 out of 399 pairs) than in normal aged AT2\_q4 cells (4 out of 71 pairs), suggesting that senescent cells might trigger forward-loops that exacerbate disease pathology. However, these autocrine loops are different under different senescence inductions (aging, chronic lung diseases, and COVID-19) even for the same cell type (Figure 3B). These findings suggest that SenCID can effectively identify senescent cells in complex tissue environments and reveal their potential contribution to age-related and disease-related changes.

To observe the continuous progression of senescence at the single-cell level, we construct trajectories of AT2 cells using

diffusion maps with SID2-related in BT-D (SID2-up and SID2-down, STAR Methods). The embeddings of the trajectories clearly track along with SID2 scores (Figure 3C) and the partition of age groups or disease origins (Figure 3D), with gene expression patterns dynamically changing at different pseudo-time points (Figure S5D). Notably, cell junction and lysosome compositions are commonly enriched in the endpoint of all trajectories, while genes related to cell respiration and active transportation are transiently elevated in the middle of trajectories, common to aging, chronic lung diseases, and COVID-19 (Figure 3E; Table S5). On the contrary, genes that are downregulated along the trajectory do not show consistent patterns across different senescence inductions, indicating that senescent cells under different conditions may lose different gene functions. For example, clathrin-coated vesicle, ribosome, or specific amino acid activation functions are specifically lost during aging, chronic lung diseases and COVID-19, respectively (Figure 3E). These findings suggest that SID2 is a reliable marker for tracking the progression of senescence in AT2 cells and that despite a common endpoint of senescence, the functions lost during different stresses are different.

We conduct an analysis of the changing patterns of transcription factor (TF) regulons along the senescent trajectories (Figure 3F). Consistent with common upregulated functions across different senescence inductions, we observe that the four trajectories exhibit many common upregulated regulons such as inflammation-responsive TFs (CEBPD, SPI1); interferon system (IRF1, STAT family); and other stress-induced factors (ENO1, JUN), being characteristic features of senescent AT2 cells in all cases. The downregulated and transiently up (intermediate) TFs, however, are more heterogeneous. Notably, the trajectory of normal aging-senescence did not exhibit the downregulation of CHD2, ELF1, and IKZF1 regulons, as well as the transient up-regulation patterns of many factors such as CREB/p300 and CLOCK, suggestive of a role in circadian regulation in disease induced senescence but not in normal aging conditions. These findings suggest that different inductions of senescence of the same cell types might be mediated through different regulations.

### SenCID reveals heterogeneous single-cell senescence trajectories during multiple tissue aging and diseases

We extend the application of SenCID to detect senescent cells in multiple tissues during aging and aging-related diseases.<sup>108–111</sup> Our results demonstrate that SenCID can accurately distinguish aged or damaged tissues from their controls with high significance and AUCs (Figures S6 and S7), for example, chondrocytes

(B) Circos plot displaying the top 50 protein-protein interactions that differ significantly between most senescent (AT2\_q4) and least senescent AT2 cells (AT2\_q1) in patients with normal aging (left), IPF (middle), and COVID-19 (right). The expression of proteins is indicated by the outer ring, while the cell types are represented by the inner ring. The line widths correspond to the absolute value of log fold changes, and line colors indicate the sign. The color intensity of lines represents significance, all with  $p < 0.05$  (Wilcoxon test). Autocrine pairs are highlighted by red font.

(C) Trajectories of AT2 cells constructed by diffusion map based on SID2-up and SID2-down gene sets, colored by SID2 scores. Senescent trajectories are indicated by gam-smoothed lines.

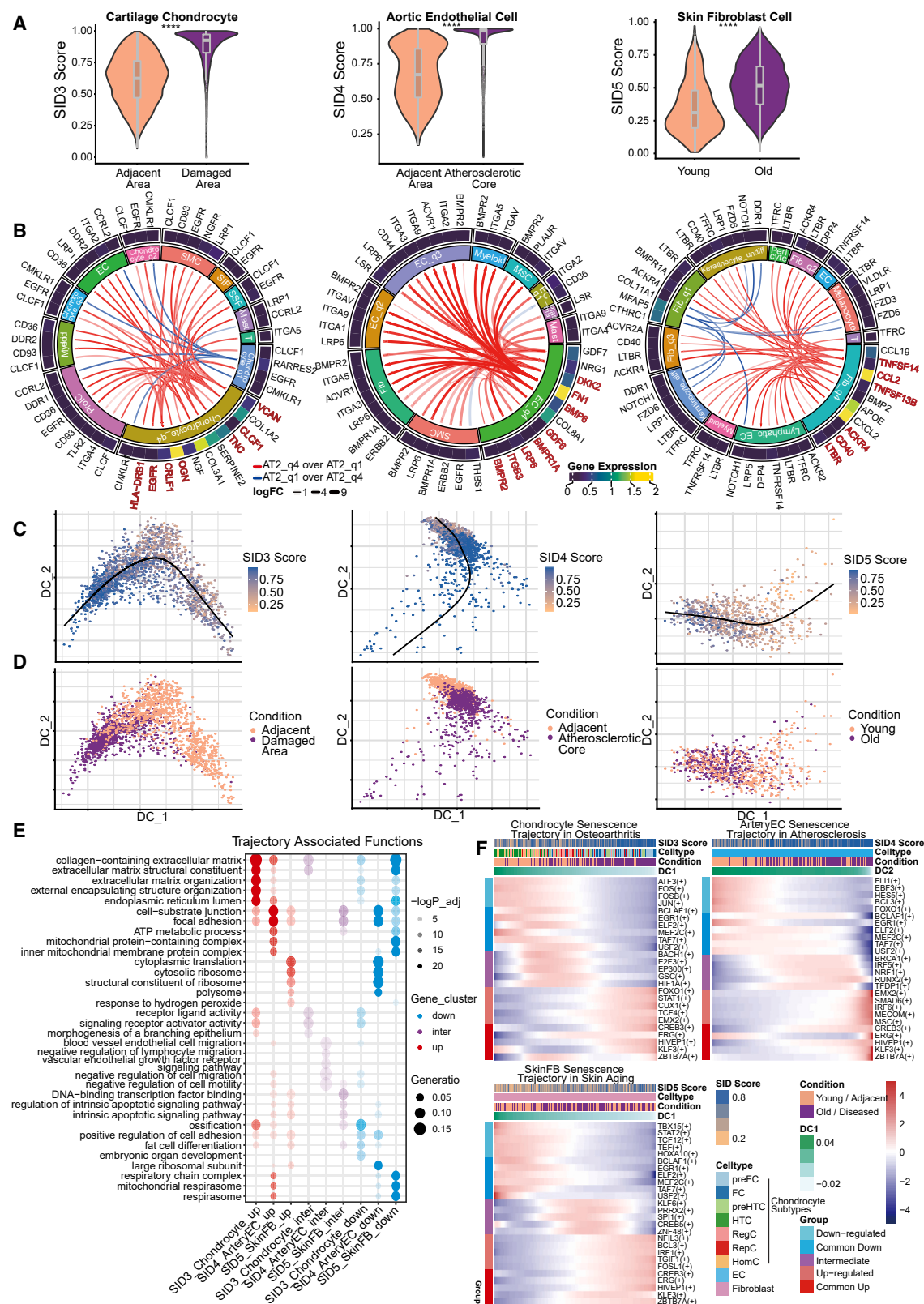
(D) Same trajectories in (C) colored by age groups or disease states.

(E) GO terms enriched from the upregulated, intermediate, and downregulated gene groups along the senescent trajectory in (C). The top 5 terms ranked by  $-\log$  BH-corrected  $p$  for each group are shown.

(F) Heatmaps of regulons with similar dynamic patterns along the trajectories. Row-scaled gam-smoothed regulon activities are indicated by the main color bar. Only upregulated regulons with significant upregulations in all four trajectories are displayed, while downregulated and intermediate regulons with common patterns in at least three trajectories are presented.

See also Figure S5.





(legend continued on next page)



(SID3) in osteoarthritis, aortic endothelial cells (ECs, SID4) in atherosclerosis, and fibroblasts (SID5) in skin aging (Figure 4A). Similar to senescent AT2 cells, these cells with highest SID scores (Cell\_q4) have significantly higher level in various cell-cell interactions than those with bottom SID scores (Cell\_q1). Among them, there are again an increase in autocrine interactions to the same cell types (40/383 pairs for chondrocytes in osteoarthritis, e.g., VCAN-EGFR related to extracellular matrix; 26/385 pairs for aortic ECs in atherosclerosis, e.g., DKK2-LRP6 related to WNT pathway<sup>112</sup>; and 10/143 pairs for normal aged skin fibroblasts, e.g., CCL2-ACKR4 related to chemokine signaling) (Figure 4B; Table S4).

We construct senescent trajectories for these different cell types using their respective SID-related senescent markers in BTD (SID3/4/5-ups and SID3/4/5-downs) (Figure 4C), which also track along the partition of disease states or age groups (Figure 4D). We find distinct gene expression patterns along the trajectories among cells from different SIDs (Figures 4E and S6C). Senescent chondrocytes (SID3) in osteoarthritis upregulate extracellular matrix-related genes and downregulate differentiation and development-related genes. Cells in the intermediate stage of the trajectory highly expressed genes related to ligand-receptor activity, which may promote chondrocyte senescence through cell-cell interactions. Aortic ECs (SID4) upregulate genes related to mitochondrial respirasome and downregulate ribosome-related genes along the trajectory, whereas skin fibroblasts (SID5) downregulate genes related to respirasome and upregulate ribosomal proteins and oxidative stress response. Transient-up genes (intermediate) are enriched in endothelial cell migration/growth factor signaling for aortic ECs and TF binding/apoptosis regulation for skin fibroblasts, respectively. These results highlight the heterogeneity of senescence initiation and endpoint in different tissues and under different stress conditions.

The patterns of TF regulons along the senescent trajectories also exhibit variations, such as the upregulation of FOXO1 regulon in chondrocyte senescence but downregulation in EC senescence in atherosclerosis, both showing high linearity (Figure 4F). On the other hand, several TF regulons display similar patterns across chondrocytes (SID3) in osteoarthritis, aortic ECs (SID4) in atherosclerosis, and fibroblasts (SID5) in skin aging trajectories. Notably, among them, ZBTB7A regulon also shares the same upregulation in all the lung epithelial cell AT2 senescent trajectories, and USF2 regulon shares the same downregulation in three of the four (except the COVID-19) AT2 senescent trajectories (Figure 3F). While there is no previous evidence supporting

the broad senescence features of these two factors, they have been primarily reported to induce senescence in prostate cancer and repress senescence in mice primary tail fibroblast cells, respectively,<sup>113,114</sup> which is consistent with our findings. Overall, the various senescence trajectories revealed by SenCID highlight the dynamics and heterogeneity of senescence trajectories even when sharing common end points.

Consistent with the notion that senescence as a progressive process toward an endpoint,<sup>4,59</sup> the single-cell senescence trajectories show gradual increase in SID scores (Figures 2F and 3A, etc.), suggesting that it might be arbitrary to define a binarized senescent state at single-cell level. However, to give an intuitive yes-or-no judgment, one can estimate a threshold for the SID scores to binarize the senescent states, where the senescence-up genes begin to increase sharply along a senescence trajectory (STAR Methods). The expression increase of these upregulated genes often accelerates around the endpoint of the trajectories (e.g., Figures S5D and S6C). In the skin fibroblast trajectory, we identified the elbow point of this acceleration, corresponding to a SID score around 0.549 (Figure S6D), which is close to 0.5, the cutoff employed to classify the senescent samples in bulk-seq data. Application of threshold 0.5 reveals an estimated senescence ratio of 53.2% for aged skin samples (Figure S6E), consistent with the reported 20%–60% senescent range of geriatric sun-protected skin fibroblasts.<sup>40,115</sup> Moreover, the threshold of 0.5-derived senescent cell ratios in Chan et al.'s data (GEO: GSE175533) is nearly perfectly linear to SA- $\beta$ -gal staining signals,<sup>104</sup> with a regression slope of 0.986 and p value of 0.00028, indicating its ability to faithfully binarize the senescent state (Figure 2F). The same method on AT2 senescent trajectories gives similar thresholds close to 0.5 (0.496 from COVID19 trajectory and 0.485 from IPF trajectory, Figures S6F and S6G). Meanwhile, using the threshold 0.5, we find all the normal control samples, even those from aged individuals, have low abundance of senescent AT2 cells (<5%, Figure S6H), consistent with the reported quantification in mouse lungs.<sup>116</sup> Thus, a binarization option for labeling senescent cells at SID score of 0.5 is provided in the SenCID program.

### SenCID enables genome-wide mapping of senescence triggers and suppressors from single-cell perturbation data

Next, we investigate whether SenCID can be used in high-throughput single-cell CRISPR screens, such as CROP-seq<sup>117,118</sup> or Perturb-seq<sup>119,120</sup> to identify genome-wide senescence trigger and suppressor genes. To test this, we apply

(B) Circos plot displaying the top 50 protein-protein interactions that differ significantly between most senescent (Cell\_q4) and least senescent cells (Cell\_q1) of cartilage chondrocytes of osteoarthritis (left), aortic ECs of atherosclerosis (middle), and skin fibroblasts of aged (right) human tissues. Annotations are the same as in Figure 3B.

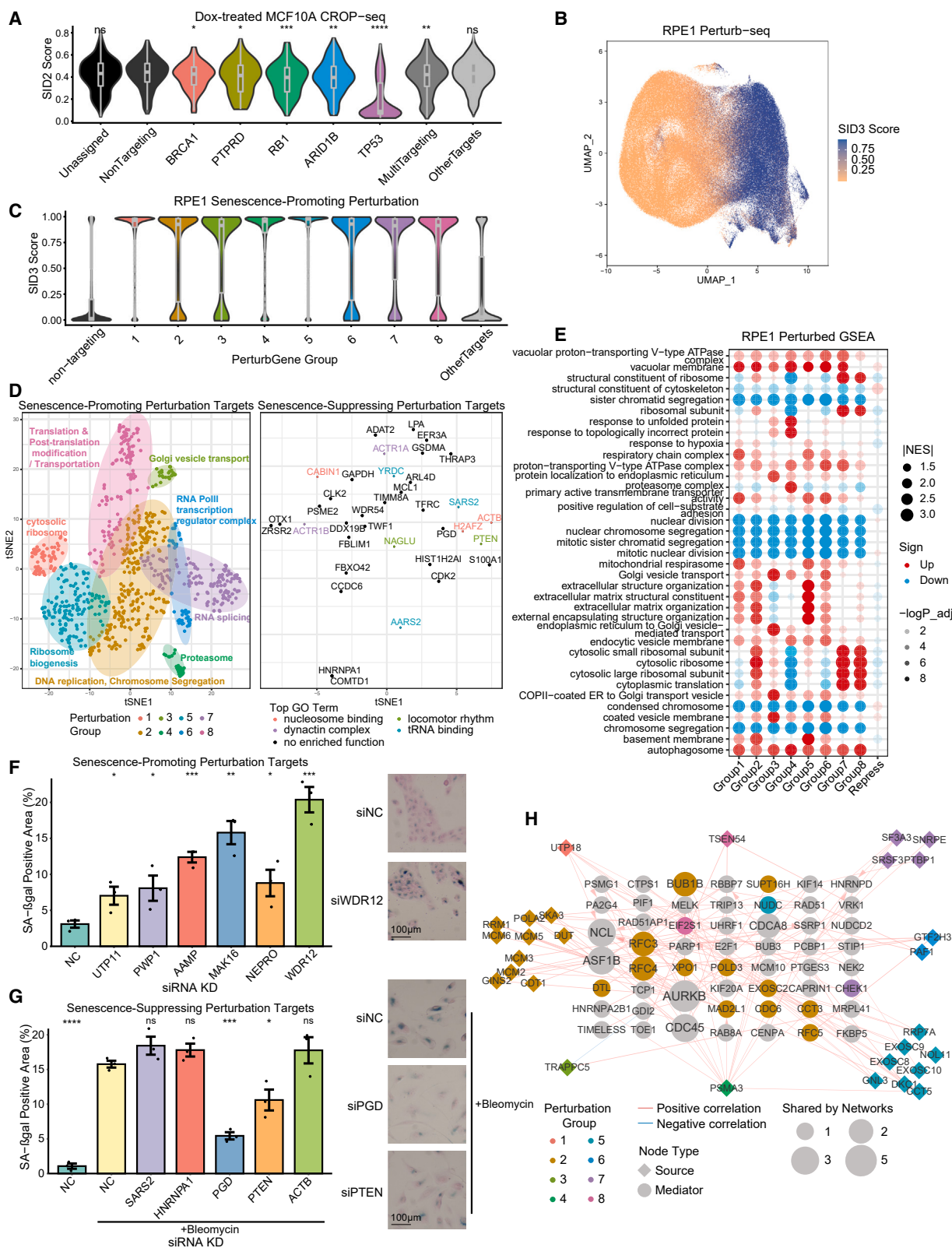
(C) Trajectories constructed by diffusion map of cartilage chondrocytes based on SID3-up and SID3-down gene sets (left), aortic ECs based on SID4-up and SID4-down gene sets (middle), and skin fibroblasts based on SID5-up and SID5-down gene sets (right), colored by their respective SID scores. Senescent trajectories are indicated by gam-smoothed lines of dot coordinates.

(D) Same trajectories in (C) colored by disease states or age groups.

(E) GO terms enriched in the upregulated, intermediate, and downregulated gene groups along the senescent trajectory in (C). The top 5 terms ranked by  $-\log$  BH-corrected p for each group are shown.

(F) Heatmaps of regulons with specific and similar dynamic patterns along trajectories. Row-scaled gam-smoothed regulon activities are indicated by the main color bar. Upregulated and downregulated regulons with top 5 significant linearity (minimum BH-corrected ANOVA p for parametric effects), intermediate regulons with top 5 significant non-linearity (minimum BH-corrected ANOVA p for non-parametric effects), and up- and downregulated regulons with significant common patterns in all three trajectories.

See also Figures S6 and S7.



(legend on next page)

SenCID to CROP-seq data from the MCF10A immortalized breast epithelial cell line,<sup>118</sup> which is a SID2 cell type according to our classification (Figures S8A and S8B). Our analysis shows a significant increase in senescence probabilities in cells treated with DNA-damaging reagents (Figures S8C and S8D), while knockdown of tumor suppressor, particularly TP53, leads to a significant decrease in SID scores (Figure 5A). These findings confirm that SenCID can capture changes in senescence levels induced by chemical treatment or gene editing in single cells. We further apply SenCID to Perturb-seq datasets from single retinal pigment epithelial cells (RPE1) and chronic myeloid leukemia cells (K562) with thousands of genes individually silenced.<sup>120</sup>

We used RPE1 cells are classified as SID3 (Figure S8E, same as in BT, Figure 1B) and exhibit an overall senescence rate of 38.3% in perturbed cells compared with 18.8% in non-targeted control cells (Figures 5B, 5C, and S8F). We identify 839 senescence-promoting and 36 senescence-suppressing genetic perturbations (Figures S8G and S8H, STAR Methods), with the senescence-promoting perturbations targeting mainly 8 groups of different essential cellular machineries, including the cytosolic ribosome, ribosome biogenesis, DNA replication and chromosome segregation, proteasome, RNA splicing, RNA polymerase II transcription regulator complex, Golgi vesicle transport, and protein translation and post-translation modification and transports. These perturbations induce senescence through similar changes to transcription profiles within the same functional group (Figure 5D). Gene set enrichment analysis (GSEA) reveals senescence-related functional terms, such as commonly reduced chromosome segregation and elevated lysosome components and autophagy, and different changing patterns of stress responses and ribosomal proteins (Figure 5E; Table S6). The senescence-suppressing perturbed genes are scattered in various functions (Figure 5D) and induce opposite, though not-so-strong effects, compared with the senescence-promoting groups (Figure 5E; Table S6).

To validate the identified senescence triggers and suppressors, we did SA- $\beta$ -gal staining experiment on a similar normal RPE1 cell line, ARPE19. Consistent with our SenCID result, we found that knocking down of the top 6 senescence-promoting perturbation targets significantly increased number of cells pos-

itive for SA- $\beta$ -gal staining (Figures 5F, S8I, and S8J), while two of the top senescence-suppressing perturbation targets, phosphogluconate dehydrogenase (PGD) and PTEN, when knocking down ameliorated the SA- $\beta$ -gal elevation induced by bleomycin (Figures 5G, S8I, and S8J).

In order to decipher the molecular pathways mediating the perturbations to senescence signatures, we employ eResponseNet analysis,<sup>121</sup> which identifies subnetworks with the largest information flow between the source and effect gene sets (STAR Methods). Using all eight groups of senescence-promoting perturbed genes as the source, we find that the largest subnetwork from eResponseNet primarily contains group 2 perturbed genes (Figures 5D and S8K), indicating that group 2 perturbations are the most direct cause of senescence. This is further supported by individual eResponseNets for each perturbation group, which show many group 2 genes as mediators (Figures 5H and S9A). The top enriched functions of all eight eResponseNets are DNA replication and chromosome segregation (Figure S9B), while pathways such as telomere lengthening, telomere capping, and rRNA and tRNA metabolisms are enriched when only considering the flows between perturbations and mediators (Figure S9C). Factors such as AURKB, NCL, ASF1B, and CDC45 are common mediators in multiple networks (Figures 5H and S9A). These findings suggest that group 2 genes are the central determinators for cellular senescence, while all other senescence modulator groups act through them.

K562, the p53-deficient cancer cell line, is difficult to become senescent, despite senescence-inducible by certain therapies, such as imatinib.<sup>122,123</sup> SenCID classifies it into SID6 (Figure S10A) and as expected, reveals very few senescent cells, regardless of perturbation (0.031%) or not (0%) (Figures 6A, S10A, and S10B). Only 37 perturbations are found to promote senescence (Figures 6B, S10C, and S10D), which cluster into 6 functional groups similar to those observed in RPE1 cells, except for the ESCRT complex genes forming a unique group. Different perturbation group induces DEGs commonly enriched for upregulated actin-related functions, myeloid cell activation, and downregulated cytosolic ribosomal proteins; these responses are very different from the responses observed in RPE1 cells (Figure 6C; Table S6). The difference in ribosomal protein changes between SID3 and 6 are consistently observed

#### Figure 5. SenCID analysis of Perturb-seq data

(A) Violin plot comparing SID2 scores of doxorubicin-treated MCF10A cells under different CROP-seq perturbations. Cells having multiple gene-targeting UMIs are marked as MultiTargeting, and cells perturbed with non-senescence-inhibiting perturbations are marked as OtherTargets. Significance between NonTargeting group and other groups is determined by Wilcoxon test (\* $p < 0.05$ ; \*\* $p < 0.01$ ; \*\*\* $p < 0.001$ ; \*\*\*\* $p < 0.0001$ ).

(B) UMAP visualization of Perturb-seq data of RPE1 cells based on high variable genes. Cells are colored by SID3 score.

(C) Distribution of SID3 scores of non-perturbed cells and cells perturbed by senescence-promoting perturbation groups.

(D) tSNE plot for the target genes of senescence-promoting (left) and senescence-suppressing perturbations (right). Each dot represents one perturbation, and their positions on the map are based on their effect on the cellular transcriptome. The dots are colored and circled by groups of their major gene functions.

(E) GSEA results of the transcriptome changes induced by different senescence-promoting perturbation groups and senescence-suppressing perturbations in (D). GO terms with top and bottom 5 NES scores in each perturbation group. |NES| > 1.

(F and G) SA- $\beta$ -gal staining of ARPE-19 cells transfected with siRNAs targeting senescence-promoting perturbation targets with top SID3 scores (F) and senescence-suppressing perturbation targets with bottom SID3 scores (G) in (D), with or without induction with 20  $\mu$ g/mL bleomycin. Quantifications of SA- $\beta$ -gal positive percentage (left) and representative images (right) are shown. Significance between 3 perturbation and control biological replicates is determined by two-tailed Student's t test (\* $p < 0.05$ ; \*\* $p < 0.01$ ; \*\*\* $p < 0.001$ ; \*\*\*\* $p < 0.0001$ ).

(H) Summary of source and mediator genes from each senescence-promoting perturbation group-initiated eResponseNet of RPE1 cells. Nodes are colored by the senescence-promoting perturbation target gene group in (D). Line colors show the signs of Pearson correlation between genes. Size of the round nodes (mediators resulted from eResponseNet) shows the number of networks in which it is a mediator.

See also Figures S8 and S9.

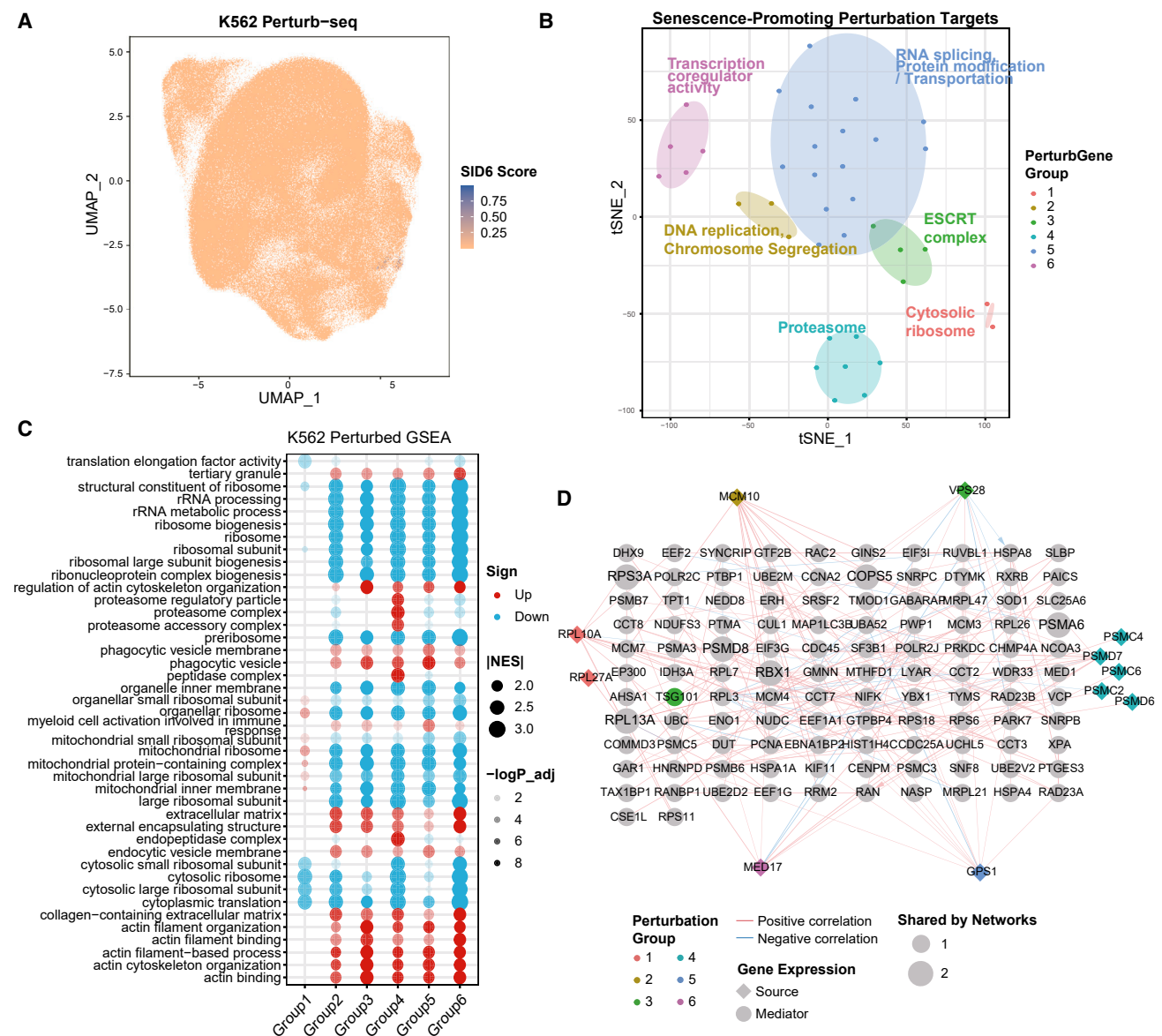


**Figure 6. SenCID analysis of Perturb-seq data in K562 cells**

(A) UMAP visualization of Perturb-seq data of K562 cells based on high variable genes, with cells colored by SID6 score.

(B) tSNE plot for the target genes of senescence-promoting perturbations on K562 cell line. Each dot represents one perturbation, and their positions on the map are based on their effect on the cellular transcriptome. The dots are colored and circled by groups of their major gene functions.

(C) GO terms with top and bottom 7 GSEA NES scores for each perturbation group. Only [NES] > 1.5 and p<sub>adj</sub> (BH-corrected p) < 0.05 terms are presented.

(D) Summary of source and mediator genes from each senescence-promoting perturbation group-initiated eResponseNet of K562 cells. Nodes are colored by the senescence-promoting perturbation target gene group in (B). Format is the same as in Figure 5F.

See also Figure S10.

in BTD (Figure 1D). Notably, unlike in RPE1 cells, different senescence-promoting perturbation groups in K562 cells elicit nearly no overlap in eResponseNet flows, with their mediators enrich for different functions (Figures 6D and S10E). Nevertheless, the most commonly enriched functions of the eResponseNet nodes are ribosomal function related (Figures S10F and S10G), indicating that ribosomal function decline is a central pathway for senescence in SID6 cells, where cell cycle checkpoint genes like p53 are disabled (Figures S3F and S10H).

## DISCUSSION

In summary, our SenCID program is an innovative machine learning algorithm capable of identifying senescence in both bulk and single-cell transcriptome data. It quantitatively assesses senescence states and heterogeneity in cell lines or primary tissues in aging and aging-related diseases. Our models reveal that cells can be classified into six different SID categories, with differing baselines of senescence inversely correlated to



stemness, distinct senescence signatures, and varying responses to senolytics. SenCID also enables the dissection of heterogeneity and reconstruction of senescent trajectories and has uncovered potential regulons for chronic human diseases, normal human tissue aging, and COVID-19. We have found that senescent cells in each pathological condition not only upregulate SASP genes to influence other cells but also enhance SASP autocrine loop, as found in multiple previous studies,<sup>124–127</sup> further highlighting the potential for self-perpetuating regulation as a target for breaking the vicious cycle of cell senescence, similar to the case for fibrosis.<sup>128</sup> Lastly, our analysis of single-cell Perturb-seq data reveals that senescence can be induced by the disruption of eight essential cellular machineries, with the majority of senescence-promoting perturbations channeled through cell cycle and chromatin-segregation-related group 2 to induce senescence. Our findings indicate a clear modularity and hierarchy among senescence modulators.

Our study provides deep insights into the ubiquity and complexity of senescence in human tissues during aging and diseases, revealing the fundamental relationship between basal senescence level and stemness and elucidating the modular nature of senescence triggers converging on a core module leading to similar senescence endpoints. Importantly, our SenCID tool allows characterizing senescent patterns that are specific to certain disease and aging processes, tissues, and cells. Such patterns have the potential to become senolytic targets if further verified to be uniquely associated with senescence in at least one cell type and absent in all others. Therefore, our findings and program have practical implications for the development of targeted senolytics to minimize off-target effects on normal cells and maximize therapeutic efficacy.

### Limitations of the study

Currently, Perturb-seq is performed on immortalized or cancer cell lines,<sup>129</sup> and thus, few or no cells undergoing senescence before perturbation, biasing our analysis toward identifying senescence triggers than suppressors. Thus, fold changes of SID scores in senescence-suppressing perturbations are much lower than the promoting perturbations. Consistently, compared with 6 out of 6 experimentally validated senescence-promoting perturbations, only 2 out of the 5 experimentally tested suppressing perturbations were validated under bleomycin induced senescence. This could also be due to a lack of full coverage of senescence-induction conditions by bleomycin treatment. Future Perturb-seq on primary cells under various senescence inductions would reveal a more complete picture of senescence suppressors. Nevertheless, we still can identify two experimental validated senescence-suppressing targets from the current dataset. One of which, PTEN, is a well-known anti-cancer gene that inhibits cell growth. While the other, PGD, is a crucial enzyme in the oxidative pentose phosphate pathway. Multiple studies regard PGD as an anti-cancer target as PGD downregulation selectively inhibits the growth of various cancer cells through AMPK pathway,<sup>130–132</sup> but no research has studied its regulation of senescence in normal, non-tumor cells. Our results show that knocking down PGD significantly reduced senescence at least in SID3 normal RPE1 cells. This indicates that PGD reduction might have dual effect of anti-cancer and anti-senescence, making it an interesting target for future study.

### STAR★METHODS

Detailed methods are provided in the online version of this paper and include the following:

- **KEY RESOURCES TABLE**
- **RESOURCE AVAILABILITY**
  - Lead contact
  - Materials availability
  - Data and code availability
- **EXPERIMENTAL MODELS**
  - Cell culture and treatment
- **METHOD DETAILS**
  - siRNA transfection
  - Senescence-associated  $\beta$ -galactosidase staining and quantitation
  - Data collection and pre-processing
  - Machine learning and non-machine learning-based senescence estimator
  - SenCID package construction
  - RNA-seq data analysis and gene set enrichment
  - Single cell analysis
  - eResponseNet network analysis
- **QUANTIFICATION AND STATISTICAL ANALYSIS**

### SUPPLEMENTAL INFORMATION

Supplemental information can be found online at <https://doi.org/10.1016/j.cmet.2024.03.009>.

### ACKNOWLEDGMENTS

This work was supported by grants from the National Natural Science Foundation of China (92374207, 92049302, 32088101, and 32330017) and the China Ministry of Science and Technology (2020YFA0804000) to J.-D.J.H.

### AUTHOR CONTRIBUTIONS

J.-D.J.H. conceived the project. W.T. performed all analysis under the guidance of J.-D.J.H., and Z.Y. helped with figure design. J.-D.J.H. and W.T. wrote the manuscript.

### DECLARATION OF INTERESTS

The authors declare no competing interests.

Received: August 18, 2023

Revised: December 15, 2023

Accepted: March 13, 2024

Published: April 10, 2024

### REFERENCES

1. Hayflick, L., and Moorhead, P.S. (1961). The serial cultivation of human diploid cell strains. *Exp. Cell Res.* 25, 585–621. [https://doi.org/10.1016/0014-4827\(61\)90192-6](https://doi.org/10.1016/0014-4827(61)90192-6).
2. Di Micco, R., Krizhanovsky, V., Baker, D., and d'Adda di Fagagna, F. (2021). Cellular senescence in ageing: from mechanisms to therapeutic opportunities. *Nat. Rev. Mol. Cell Biol.* 22, 75–95. <https://doi.org/10.1038/s41580-020-00314-w>.
3. von Zglinicki, T., Wan, T., and Miwa, S. (2021). Senescence in Post-Mitotic Cells: A Driver of Aging? *Antioxid. Redox Signal.* 34, 308–323. <https://doi.org/10.1089/ars.2020.8048>.



4. van Deursen, J.M. (2014). The role of senescent cells in ageing. *Nature* 509, 439–446. <https://doi.org/10.1038/nature13193>.
5. Coppé, J.P., Patil, C.K., Rodier, F., Sun, Y., Muñoz, D.P., Goldstein, J., Nelson, P.S., Desprez, P.Y., and Campisi, J. (2008). Senescence-Associated Secretory Phenotypes Reveal Cell-Nonautonomous Functions of Oncogenic RAS and the p53 Tumor Suppressor. *PLOS Biol.* 6, 2853–2868. <https://doi.org/10.1371/journal.pbio.0060301>.
6. Rodier, F., and Campisi, J. (2011). Four faces of cellular senescence. *J. Cell Biol.* 192, 547–556. <https://doi.org/10.1083/jcb.201009094>.
7. Gorgoulis, V., Adams, P.D., Alimonti, A., Bennett, D.C., Bischof, O., Bishop, C., Campisi, J., Collado, M., Evangelou, K., Ferbeyre, G., et al. (2019). Cellular Senescence: Defining a Path Forward. *Cell* 179, 813–827. <https://doi.org/10.1016/j.cell.2019.10.005>.
8. He, S., and Sharpless, N.E. (2017). Senescence in Health and Disease. *Cell* 169, 1000–1011. <https://doi.org/10.1016/j.cell.2017.05.015>.
9. Childs, B.G., Baker, D.J., Wijshake, T., Conover, C.A., Campisi, J., and van Deursen, J.M. (2016). Senescent intimal foam cells are deleterious at all stages of atherosclerosis. *Science* 354, 472–477. <https://doi.org/10.1126/science.aaf6659>.
10. Childs, B.G., Zhang, C., Shuja, F., Sturmlechner, I., Trewartha, S., Fierro Velasco, R.F., Baker, D.J., Li, H., and van Deursen, J.M. (2021). Senescent cells suppress innate smooth muscle cell repair functions in atherosclerosis. *Nat. Aging* 1, 698–714. <https://doi.org/10.1038/s43587-021-00089-5>.
11. Borghesan, M., Hoogaars, W.M.H., Varela-Eirin, M., Talma, N., and Demaria, M. (2020). A Senescence-Centric View of Aging: Implications for Longevity and Disease. *Trends Cell Biol.* 30, 777–791. <https://doi.org/10.1016/j.tcb.2020.07.002>.
12. Baker, D.J., Childs, B.G., Durik, M., Wijers, M.E., Sieben, C.J., Zhong, J., Saltness, R.A., Jeganathan, K.B., Verzoza, G.C., et al. (2016). Naturally occurring p16Ink4a-positive cells shorten healthy lifespan. *Nature* 530, 184–189. <https://doi.org/10.1038/nature16932>.
13. Baker, D.J., Wijshake, T., Tchkonja, T., LeBrasseur, N.K., Childs, B.G., van de Sluis, B., Kirkland, J.L., and van Deursen, J.M. (2011). Clearance of p16Ink4a-positive senescent cells delays ageing-associated disorders. *Nature* 479, 232–236. <https://doi.org/10.1038/nature10600>.
14. Song, S., Lam, E.W., Tchkonja, T., Kirkland, J.L., and Sun, Y. (2020). Senescent Cells: Emerging Targets for Human Aging and Age-Related Diseases. *Trends Biochem. Sci.* 45, 578–592. <https://doi.org/10.1016/j.tibs.2020.03.008>.
15. Chaib, S., Tchkonja, T., and Kirkland, J.L. (2022). Cellular senescence and senolytics: the path to the clinic. *Nat. Med.* 28, 1556–1568. <https://doi.org/10.1038/s41591-022-01923-y>.
16. Reyes, N.S., Krasilnikov, M., Allen, N.C., Lee, J.Y., Hyams, B., Zhou, M., Ravishanker, S., Cassandras, M., Wang, C., Khan, I., et al. (2022). Sentinel p16INK4a+ cells in the basement membrane form a reparative niche in the lung. *Science* 378, 192–201. <https://doi.org/10.1126/science.abf3326>.
17. Hernandez-Segura, A., de Jong, T.V., Melov, S., Guryev, V., Campisi, J., and Demaria, M. (2017). Unmasking Transcriptional Heterogeneity in Senescent Cells. *Curr. Biol.* 27, 2652–2660.e4. <https://doi.org/10.1016/j.cub.2017.07.033>.
18. Zhu, Y., Dornebal, E.J., Pirtskhalava, T., Giorgadze, N., Wentworth, M., Fuhrmann-Stroissnigg, H., Niedernhofer, L.J., Robbins, P.D., Tchkonja, T., and Kirkland, J.L. (2017). New agents that target senescent cells: the flavone, fisetin, and the BCL-X(L) inhibitors, A1331852 and A1155463. *Aging (Albany, NY)* 9, 955–963. <https://doi.org/10.18632/aging.101202>.
19. Gil, J. (2023). The challenge of identifying senescent cells. *Nat. Cell Biol.* 25, 1554–1556. <https://doi.org/10.1038/s41556-023-01267-w>.
20. Lee, B.Y., Han, J.A., Im, J.S., Morrone, A., Johung, K., Goodwin, E.C., Kleijer, W.J., DiMaio, D., and Hwang, E.S. (2006). Senescence-associated beta-galactosidase is lysosomal beta-galactosidase. *Aging Cell* 5, 187–195. <https://doi.org/10.1111/j.1474-9726.2006.00199.x>.
21. Schwartz, R.E., Shokhirev, M.N., Andrade, L.R., Gutkind, J.S., Iglesias-Bartolome, R., and Shadel, G.S. (2021). Insights into epithelial cell senescence from transcriptome and secretome analysis of human oral keratinocytes. *Aging (Albany, NY)* 13, 4747–4777. <https://doi.org/10.18632/aging.202658>.
22. Avelar, R.A., Ortega, J.G., Tacutu, R., Tyler, E.J., Bennett, D., Binetti, P., Budovsky, A., Chatsirisupachai, K., Johnson, E., Murray, A., et al. (2020). A multidimensional systems biology analysis of cellular senescence in aging and disease. *Genome Biol.* 21, 91. <https://doi.org/10.1186/s13059-020-01990-9>.
23. Chatsirisupachai, K., Palmer, D., Ferreira, S., and de Magalhães, J.P. (2019). A human tissue-specific transcriptomic analysis reveals a complex relationship between aging, cancer, and cellular senescence. *Aging Cell* 18, e13041. <https://doi.org/10.1111/accel.13041>.
24. Zhao, M., Chen, L., and Qu, H. (2016). CSGene: a literature-based database for cell senescence genes and its application to identify critical cell aging pathways and associated diseases. *Cell Death Dis.* 7, e2053. <https://doi.org/10.1038/cddis.2015.414>.
25. Reyfman, P.A., Walter, J.M., Joshi, N., Anekalla, K.R., McQuattie-Pimentel, A.C., Chiu, S., Fernandez, R., Akbarpour, M., Chen, C.I., Ren, Z., et al. (2019). Single-Cell Transcriptomic Analysis of Human Lung Provides Insights into the Pathobiology of Pulmonary Fibrosis. *Am. J. Respir. Crit. Care Med.* 199, 1517–1536. <https://doi.org/10.1164/rccm.201712-2410OC>.
26. Wang, X., Ma, L., Pei, X., Wang, H., Tang, X., Pei, J.F., Ding, Y.N., Qu, S., Wei, Z.Y., Wang, H.Y., et al. (2022). Comprehensive assessment of cellular senescence in the tumor microenvironment. *Brief. Bioinform.* 23, bbac118. <https://doi.org/10.1093/bib/bbac118>.
27. Jochems, F., Thijssen, B., De Conti, G., Jansen, R., Pogacar, Z., Groot, K., Wang, L., Schepers, A., Wang, C., Jin, H., et al. (2021). The Cancer SENESCopedia: A delineation of cancer cell senescence. *Cell Rep.* 36, 109441. <https://doi.org/10.1016/j.celrep.2021.109441>.
28. Gulati, G.S., Sikandar, S.S., Wesche, D.J., Manjunath, A., Bharadwaj, A., Berger, M.J., Ilagan, F., Kuo, A.H., Hsieh, R.W., Cai, S., et al. (2020). Single-cell transcriptional diversity is a hallmark of developmental potential. *Science* 367, 405–411. <https://doi.org/10.1126/science.aax0249>.
29. Malta, T.M., Sokolov, A., Gentles, A.J., Burzykowski, T., Poisson, L., Weinstein, J.N., Kamińska, B., Huelsenken, J., Omberg, L., Gevaert, O., et al. (2018). Machine Learning Identifies Stemness Features Associated with Oncogenic Dedifferentiation. *Cell* 173, 338–354.e15. <https://doi.org/10.1016/j.cell.2018.03.034>.
30. Guo, M., Bao, E.L., Wagner, M., Whitsett, J.A., and Xu, Y. (2017). SLICE: determining cell differentiation and lineage based on single cell entropy. *Nucleic Acids Res.* 45, e54. <https://doi.org/10.1093/nar/gkw1278>.
31. Teschendorff, A.E., and Enver, T. (2017). Single-cell entropy for accurate estimation of differentiation potency from a cell's transcriptome. *Nat. Commun.* 8, 15599. <https://doi.org/10.1038/ncomms15599>.
32. Grün, D., Muraro, M.J., Boisset, J.C., Wiebrands, K., Lyubimova, A., Dharmadhikari, G., van den Born, M., van Es, J., Jansen, E., Clevers, H., et al. (2016). De Novo Prediction of Stem Cell Identity using Single-Cell Transcriptome Data. *Cell Stem Cell* 19, 266–277. <https://doi.org/10.1016/j.stem.2016.05.010>.
33. Kim, S., and Kim, C. (2021). Transcriptomic Analysis of Cellular Senescence: One Step Closer to Senescence Atlas. *Mol. Cells* 44, 136–145. <https://doi.org/10.14348/molcells.2021.2239>.
34. Cohn, R.L., Gasek, N.S., Kuchel, G.A., and Xu, M. (2023). The heterogeneity of cellular senescence: insights at the single-cell level. *Trends Cell Biol.* 33, 9–17. <https://doi.org/10.1016/j.tcb.2022.04.011>.
35. Sati, S., Bonev, B., Szabo, Q., Jost, D., Bensadoun, P., Serra, F., Loubiere, V., Papadopoulos, G.L., Rivera-Mulia, J.C., Fritsch, L., et al. (2020). 4D Genome Rewiring during Oncogene-Induced and Replicative Senescence. *Mol. Cell* 78, 522–538.e9. <https://doi.org/10.1016/j.molcel.2020.03.007>.
36. Wang, R.W., Viganò, S., Ben-David, U., Amon, A., and Santaguida, S. (2021). Aneuploid senescent cells activate NF-κB to promote their

- immune clearance by NK cells. *EMBO Rep.* 22, e52032. <https://doi.org/10.15252/embr.202052032>.
37. Wang, S., Hu, B., Ding, Z., Dang, Y., Wu, J., Li, D., Liu, X., Xiao, B., Zhang, W., Ren, R., et al. (2018). ATF6 safeguards organelle homeostasis and cellular aging in human mesenchymal stem cells. *Cell Discov.* 4, 2. <https://doi.org/10.1038/s41421-017-0003-0>.
38. Kovatcheva, M., Liao, W., Klein, M.E., Robine, N., Geiger, H., Crago, A.M., Dickson, M.A., Tap, W.D., Singer, S., and Koff, A. (2017). ATRX is a regulator of therapy induced senescence in human cells. *Nat. Commun.* 8, 386. <https://doi.org/10.1038/s41467-017-00540-5>.
39. Mongiardi, M.P., Radice, G., Piras, M., Stagni, V., Pacioni, S., Re, A., Putti, S., Ferrè, F., Farsetti, A., Pallini, R., et al. (2019). Axitinib exposure triggers endothelial cells senescence through ROS accumulation and ATM activation. *Oncogene* 38, 5413–5424. <https://doi.org/10.1038/s41388-019-0798-2>.
40. Lämmermann, I., Terlecki-Zaniewicz, L., Weinmüller, R., Schosserer, M., Dellago, H., de Matos Branco, A.D., Authier, D., Sevcnikar, B., Kleissl, L., Berlin, I., et al. (2018). Blocking negative effects of senescence in human skin fibroblasts with a plant extract. *npj Aging Mech. Dis.* 4, 4. <https://doi.org/10.1038/s41514-018-0023-5>.
41. Tasdemir, N., Banito, A., Roe, J.S., Alonso-Curbelo, D., Camiolo, M., Tschaharganeh, D.F., Huang, C.H., Aksoy, O., Bolden, J.E., Chen, C.C., et al. (2016). BRD4 Connects Enhancer Remodeling to Senescence Immune Surveillance. *Cancer Discov.* 6, 612–629. <https://doi.org/10.1158/2159-8290.CD-16-0217>.
42. Crowe, E.P., Tuzer, F., Gregory, B.D., Donahue, G., Gosai, S.J., Cohen, J., Leung, Y.Y., Yetkin, E., Nativio, R., Wang, L.S., et al. (2016). Changes in the Transcriptome of Human Astrocytes Accompanying Oxidative Stress-Induced Senescence. *Front. Aging Neurosci.* 8, 208. <https://doi.org/10.3389/fnagi.2016.00208>.
43. Santaguida, S., Richardson, A., Iyer, D.R., M'Saad, O., Zasadil, L., Knouse, K.A., Wong, Y.L., Rhind, N., Desai, A., and Amon, A. (2017). Chromosome Mis-segregation Generates Cell-Cycle-Arrested Cells with Complex Karyotypes that Are Eliminated by the Immune System. *Dev. Cell* 41, 638–651.e5. <https://doi.org/10.1016/j.devcel.2017.05.022>.
44. Aarts, M., Georgilis, A., Beniazza, M., Beolchi, P., Banito, A., Carroll, T., Kulisic, M., Kaemena, D.F., Dharmalingam, G., Martin, N., et al. (2017). Coupling shRNA screens with single-cell RNA-seq identifies a dual role for mTOR in reprogramming-induced senescence. *Genes Dev.* 31, 2085–2098. <https://doi.org/10.1101/gad.297796.117>.
45. Zhao, Z., Dong, Q., Liu, X., Wei, L., Liu, L., Li, Y., and Wang, X. (2020). Dynamic transcriptome profiling in DNA damage-induced cellular senescence and transient cell-cycle arrest. *Genomics* 112, 1309–1317. <https://doi.org/10.1016/j.ygeno.2019.07.020>.
46. Wang, S., Wang, Z., Su, H., Chen, F., Ma, M., Yu, W., Ye, G., Cen, S., Mi, R., Wu, X., et al. (2021). Effects of long-term culture on the biological characteristics and RNA profiles of human bone-marrow-derived mesenchymal stem cells. *Mol. Ther. Nucleic Acids* 26, 557–574. <https://doi.org/10.1016/j.omtn.2021.08.013>.
47. Chan, K.T., Blake, S., Zhu, H., Kang, J., Trigos, A.S., Madhamshettiwar, P.B., Diesch, J., Paavola, L., Horvath, P., Hannan, R.D., et al. (2020). A functional genetic screen defines the AKT-induced senescence signaling network. *Cell Death Differ.* 27, 725–741. <https://doi.org/10.1038/s41418-019-0384-8>.
48. Purcell, M., Kruger, A., and Tainsky, M.A. (2014). Gene expression profiling of replicative and induced senescence. *Cell Cycle* 13, 3927–3937. <https://doi.org/10.4161/15384101.2014.973327>.
49. Yang, J., Li, J., Suzuki, K., Liu, X., Wu, J., Zhang, W., Ren, R., Zhang, W., Chan, P., Izpisua Belmonte, J.C., et al. (2017). Genetic enhancement in cultured human adult stem cells conferred by a single nucleotide recoding. *Cell Res.* 27, 1178–1181. <https://doi.org/10.1038/cr.2017.86>.
50. Ávila-López, P.A., Guerrero, G., Nuñez-Martínez, H.N., Peralta-Alvarez, C.A., Hernández-Montes, G., Álvarez-Hilario, L.G., Herrera-Goepfert, R., Albores-Saavedra, J., Villegas-Sepúlveda, N., Cedillo-Barrón, L., et al. (2021). H2A.Z overexpression suppresses senescence and chemo-sensitivity in pancreatic ductal adenocarcinoma. *Oncogene* 40, 2065–2080. <https://doi.org/10.1038/s41388-021-01664-1>.
51. Wang, L., Leite de Oliveira, R., Wang, C., Fernandes Neto, J.M., Mainardi, S., Evers, B., Liefink, C., Morris, B., Jochems, F., Willemsen, L., et al. (2017). High-Throughput Functional Genetic and Compound Screens Identify Targets for Senescence Induction in Cancer. *Cell Rep.* 21, 773–783. <https://doi.org/10.1016/j.celrep.2017.09.085>.
52. Saunderson, E.A., Stepper, P., Gomm, J.J., Hoa, L., Morgan, A., Allen, M.D., Jones, J.L., Gribben, J.G., Jurkowski, T.P., and Ficiz, G. (2017). Hit-and-run epigenetic editing prevents senescence entry in primary breast cells from healthy donors. *Nat. Commun.* 8, 1450. <https://doi.org/10.1038/s41467-017-01078-2>.
53. Zirkel, A., Nikolic, M., Sofiadis, K., Mallm, J.P., Brackley, C.A., Gothe, H., Drechsel, O., Becker, C., Altmüller, J., Josipovic, N., et al. (2018). HMGB2 Loss upon Senescence Entry Disrupts Genomic Organization and Induces CTCF Clustering across Cell Types. *Mol. Cell* 70, 730–744.e6. <https://doi.org/10.1016/j.molcel.2018.03.030>.
54. Marthandan, S., Priebe, S., Groth, M., Guthke, R., Platzer, M., Hemmerich, P., and Diekmann, S. (2015). Hormetic effect of rotenone in primary human fibroblasts. *Immun. Ageing* 12, 11. <https://doi.org/10.1186/s12979-015-0038-8>.
55. Birger, A., Ben-Dor, I., Ottolenghi, M., Turetsky, T., Gil, Y., Sweetat, S., Perez, L., Belzer, V., Casden, N., Steiner, D., et al. (2019). Human iPSC-derived astrocytes from ALS patients with mutated C9ORF72 show increased oxidative stress and neurotoxicity. *EBioMedicine* 50, 274–289. <https://doi.org/10.1016/j.ebiom.2019.11.026>.
56. Gu, J., Wang, J., Liu, X., Sai, K., Mai, J., Xing, F., Chen, Z., Yang, X., Lu, W., Guo, C., et al. (2021). IL-6 derived from therapy-induced senescence facilitates the glycolytic phenotype in glioblastoma cells. *Am. J. Cancer Res.* 11, 458–478.
57. Wang, C., Vegna, S., Jin, H., Benedict, B., Liefink, C., Ramirez, C., de Oliveira, R.L., Morris, B., Gadiot, J., Wang, W., et al. (2019). Inducing and exploiting vulnerabilities for the treatment of liver cancer. *Nature* 574, 268–272. <https://doi.org/10.1038/s41586-019-1607-3>.
58. Zhang, B., Long, Q., Wu, S., Xu, Q., Song, S., Han, L., Qian, M., Ren, X., Liu, H., Jiang, J., et al. (2021). KDM4 Orchestrates Epigenomic Remodeling of Senescent Cells and Potentiates the Senescence-Associated Secretory Phenotype. *Nat Aging* 1, 454–472. <https://doi.org/10.1038/s43587-021-00063-1>.
59. De Cecco, M., Ito, T., Petrashen, A.P., Elias, A.E., Skvir, N.J., Criscione, S.W., Caligiana, A., Broccoli, G., Adney, E.M., Boeke, J.D., et al. (2019). L1 drives IFN in senescent cells and promotes age-associated inflammation. *Nature* 566, 73–78. <https://doi.org/10.1038/s41586-018-0784-9>.
60. Zhang, X., Liu, X., Du, Z., Wei, L., Fang, H., Dong, Q., Niu, J., Li, Y., Gao, J., Zhang, M.Q., et al. (2021). The loss of heterochromatin is associated with multiscale three-dimensional genome reorganization and aberrant transcription during cellular senescence. *Genome Res.* 31, 1121–1135. <https://doi.org/10.1101/gr.275235.121>.
61. Ohashi, M., Korsakova, E., Allen, D., Lee, P., Fu, K., Vargas, B.S., Cinkornpumin, J., Salas, C., Park, J.C., Germanguz, I., et al. (2018). Loss of MECP2 Leads to Activation of P53 and Neuronal Senescence. *Stem Cell Rep.* 10, 1453–1463. <https://doi.org/10.1016/j.stemcr.2018.04.001>.
62. Riessland, M., Kolisnyk, B., Kim, T.W., Cheng, J., Ni, J., Pearson, J.A., Park, E.J., Dam, K., Acehan, D., Ramos-Espíritu, L.S., et al. (2019). Loss of SATB1 Induces p21-Dependent Cellular Senescence in Post-mitotic Dopaminergic Neurons. *Cell Stem Cell* 25, 514–530.e8. <https://doi.org/10.1016/j.stem.2019.08.013>.
63. Lenain, C., de Graaf, C.A., Pagie, L., Visser, N.L., de Haas, M., de Vries, S.S., Peric-Hupkes, D., van Steensel, B., and Peeper, D.S. (2017). Massive reshaping of genome-nuclear lamina interactions during oncogene-induced senescence. *Genome Res.* 27, 1634–1644. <https://doi.org/10.1101/gr.225763.117>.
64. DePianto, D.J., Heiden, J.A.V., Morshead, K.B., Sun, K.H., Modrusan, Z., Teng, G., Wolters, P.J., and Arron, J.R. (2021). Molecular mapping of

- interstitial lung disease reveals a phenotypically distinct senescent basal epithelial cell population. *JCI Insight* 6, e143626. <https://doi.org/10.1172/jci.insight.143626>.
65. Herranz, N., Gallage, S., Mellone, M., Wuestefeld, T., Klotz, S., Hanley, C.J., Raguz, S., Acosta, J.C., Innes, A.J., Banito, A., et al. (2015). mTOR regulates MAPKAPK2 translation to control the senescence-associated secretory phenotype. *Nat. Cell Biol.* 17, 1205–1217. <https://doi.org/10.1038/ncb3225>.
66. St-Jean, S., De Castro, A.C., Lecours, M., Jones, C., Rivard, N., Rodier, F., Perreault, N., and Boudreau, F. (2021). NCOR1 Sustains Colorectal Cancer Cell Growth and Protects against Cellular Senescence. *Cancers (Basel)* 13, 4414. <https://doi.org/10.3390/cancers13174414>.
67. Ruscetti, M., Leibold, J., Bott, M.J., Fennell, M., Kulick, A., Salgado, N.R., Chen, C.C., Ho, Y.J., Sanchez-Rivera, F.J., Feucht, J., et al. (2018). NK cell-mediated cytotoxicity contributes to tumor control by a cytostatic drug combination. *Science* 362, 1416–1422. <https://doi.org/10.1126/science.aas9090>.
68. Hoare, M., Ito, Y., Kang, T.W., Weekes, M.P., Matheson, N.J., Patten, D.A., Shetty, S., Parry, A.J., Menon, S., Salama, R., et al. (2016). NOTCH1 mediates a switch between two distinct secretomes during senescence. *Nat. Cell Biol.* 18, 979–992. <https://doi.org/10.1038/ncb3397>.
69. Sturmlechner, I., Zhang, C., Sine, C.C., van Deursen, E.J., Jeganathan, K.B., Hamada, N., Grasic, J., Friedman, D., Stutchman, J.T., Can, I., et al. (2021). p21 produces a bioactive secretome that places stressed cells under immunosurveillance. *Science* 374, eabb3420. <https://doi.org/10.1126/science.abb3420>.
70. Soshnikova, N.V., Tatarskiy, E.V., Tatarskiy, V.V., Klimenko, N.S., Shtil, A.A., Nikiforov, M.A., and Georgieva, S.G. (2021). PHF10 subunit of PBAF complex mediates transcriptional activation by MYC. *Oncogene* 40, 6071–6080. <https://doi.org/10.1038/s41388-021-01994-0>.
71. Wang, S., Min, Z., Ji, Q., Geng, L., Su, Y., Liu, Z., Hu, H., Wang, L., Zhang, W., Suzuki, K., et al. (2020). Rescue of premature aging defects in Cockayne syndrome stem cells by CRISPR/Cas9-mediated gene correction. *Protein Cell* 11, 1–22. <https://doi.org/10.1007/s13238-019-0623-2>.
72. Balakrishnan, I., Danis, E., Pierce, A., Madhavan, K., Wang, D., Dahl, N., Sanford, B., Birks, D.K., Davidson, N., Metselaar, D.S., et al. (2020). Senescence Induced by BMI1 Inhibition Is a Therapeutic Vulnerability in H3K27M-Mutant DIPG. *Cell Rep.* 33, 108286. <https://doi.org/10.1016/j.celrep.2020.108286>.
73. Martínez-Zamudio, R.I., Dewald, H.K., Vasilopoulos, T., Gittens-Williams, L., Fitzgerald-Bocarsly, P., and Herbig, U. (2021). Senescence-associated  $\beta$ -galactosidase reveals the abundance of senescent CD8+ T cells in aging humans. *Aging Cell* 20, e13344. <https://doi.org/10.1111/acer.13344>.
74. Marthandan, S., Priebe, S., Baumgart, M., Groth, M., Cellerino, A., Guthke, R., Hemmerich, P., and Diekmann, S. (2015). Similarities in Gene Expression Profiles during In Vitro Aging of Primary Human Embryonic Lung and Foreskin Fibroblasts. *BioMed Res. Int.* 2015, 731938. <https://doi.org/10.1155/2015/731938>.
75. Uryga, A.K., Grootaert, M.O.J., Garrido, A.M., Oc, S., Foote, K., Chappell, J., Finigan, A., Rossiello, F., d'Adda di Fagnana, F., Aravani, D., et al. (2021). Telomere damage promotes vascular smooth muscle cell senescence and immune cell recruitment after vessel injury. *Commun. Biol.* 4, 611. <https://doi.org/10.1038/s42003-021-02123-z>.
76. Zhang, X., Liu, Z., Liu, X., Wang, S., Zhang, Y., He, X., Sun, S., Ma, S., Shyh-Chang, N., Liu, F., et al. (2019). Telomere-dependent and telomere-independent roles of RAP1 in regulating human stem cell homeostasis. *Protein Cell* 10, 649–667. <https://doi.org/10.1007/s13238-019-0610-7>.
77. Kolesnichenko, M., Mikuda, N., Höpken, U.E., Kärger, E., Uyar, B., Tufan, A.B., Milanovic, M., Sun, W., Krahn, I., Schleich, K., et al. (2021). Transcriptional repression of NFKBIA triggers constitutive IKK- and proteasome-independent p65/RelA activation in senescence. *EMBO J.* 40, e104296. <https://doi.org/10.15252/embj.2019104296>.
78. Casella, G., Munk, R., Kim, K.M., Piao, Y., De, S., Abdelmohsen, K., and Gorospe, M. (2019). Transcriptome signature of cellular senescence. *Nucleic Acids Res.* 47, 7294–7305. <https://doi.org/10.1093/nar/gkz555>.
79. Lau, L., Porciuncula, A., Yu, A., Iwakura, Y., and David, G. (2019). Uncoupling the Senescence-Associated Secretory Phenotype from Cell Cycle Exit via Interleukin-1 Inactivation Unveils Its Protumorigenic Role. *Mol. Cell. Biol.* 39. <https://doi.org/10.1128/MCB.00586-18>.
80. Fu, L., Hu, Y., Song, M., Liu, Z., Zhang, W., Yu, F.X., Wu, J., Wang, S., Izpisua Belmonte, J.C., Chan, P., et al. (2019). Up-regulation of FOXD1 by YAP alleviates senescence and osteoarthritis. *PLoS Biol.* 17, e3000201. <https://doi.org/10.1371/journal.pbio.3000201>.
81. Guyon, I., Weston, J., Barnhill, S., and Vapnik, V. (2002). Gene Selection for Cancer Classification using Support Vector Machines. *Mach. Learn.* 46, 389–422. <https://doi.org/10.1023/A:1012487302797>.
82. Payea, M.J., Aneillas, C., Tharakan, R., and Gorospe, M. (2021). Translational Control during Cellular Senescence. *Mol. Cell. Biol.* 41, e00512-00520. <https://doi.org/10.1128/MCB.00512-20>.
83. Yosef, R., Pilpel, N., Tokarsky-Amiel, R., Biran, A., Ovadya, Y., Cohen, S., Vadai, E., Dassa, L., Shahar, E., Condiotti, R., et al. (2016). Directed elimination of senescent cells by inhibition of BCL-W and BCL-XL. *Nat. Commun.* 7, 11190. <https://doi.org/10.1038/ncomms11190>.
84. Chang, J., Wang, Y., Shao, L., Laberge, R.M., Demaria, M., Campisi, J., Janakiraman, K., Sharpless, N.E., Ding, S., Feng, W., et al. (2016). Clearance of senescent cells by ABT263 rejuvenates aged hematopoietic stem cells in mice. *Nat. Med.* 22, 78–83. <https://doi.org/10.1038/nm.4010>.
85. Guerrero, A., Herranz, N., Sun, B., Wagner, V., Gallage, S., Guiho, R., Wolter, K., Pombo, J., Irvine, E.E., Innes, A.J., et al. (2019). Cardiac glycosides are broad-spectrum senolytics. *Nat. Metab.* 1, 1074–1088. <https://doi.org/10.1038/s42255-019-0122-z>.
86. Xu, Q., Fu, Q., Li, Z., Liu, H., Wang, Y., Lin, X., He, R., Zhang, X., Ju, Z., Campisi, J., et al. (2021). The flavonoid procyanidin C1 has senotherapeutic activity and increases lifespan in mice. *Nat. Metab.* 3, 1706–1726. <https://doi.org/10.1038/s42255-021-00491-8>.
87. Esnault, S., Bernau, K., Torr, E.E., Bochkov, Y.A., Jarjour, N.N., and Sandbo, N. (2017). RNA-sequencing analysis of lung primary fibroblast response to eosinophil-degranulation products predicts downstream effects on inflammation, tissue remodeling and lipid metabolism. *Respir. Res.* 18, 188. <https://doi.org/10.1186/s12931-017-0669-8>.
88. Hall, B.M., Balan, V., Gleiberman, A.S., Strom, E., Krasnov, P., Virtuoso, L.P., Rydkina, E., Vujcic, S., Balan, K., Gitlin, I.I., et al. (2017). p16(Ink4a) and senescence-associated  $\beta$ -galactosidase can be induced in macrophages as part of a reversible response to physiological stimuli. *Aging (Albany, NY)* 9, 1867–1884. <https://doi.org/10.18632/aging.101268>.
89. Fuentes, L., Wouters, K., Hannou, S.A., Cudejko, C., Rigamonti, E., Mayi, T.H., Derudas, B., Pattou, F., Chinetti-Gbaguidi, G., Staels, B., and Paumelle, R. (2011). Downregulation of the tumour suppressor p16INK4A contributes to the polarisation of human macrophages toward an adipose tissue macrophage (ATM)-like phenotype. *Diabetologia* 54, 3150–3156. <https://doi.org/10.1007/s00125-011-2324-0>.
90. Walker, E.J., Heydet, D., Veldre, T., and Ghildyal, R. (2019). Transcriptomic changes during TGF- $\beta$ -mediated differentiation of airway fibroblasts to myofibroblasts. *Sci. Rep.* 9, 20377. <https://doi.org/10.1038/s41598-019-56955-1>.
91. Druzhkova, I., Shirmanova, M., Ignatova, N., Dudenkova, V., Lukina, M., Zagaynova, E., Safina, D., Kostrov, S., Didych, D., Kuzmich, A., et al. (2020). Expression of EMT-Related Genes in Hybrid E/M Colorectal Cancer Cells Determines Fibroblast Activation and Collagen Remodeling. *Int. J. Mol. Sci.* 21, 8119. <https://doi.org/10.3390/ijms21218119>.
92. Park, H.J., Hoffman, J.R., Brown, M.E., Bheri, S., Brazhkina, O., Son, Y.H., and Davis, M.E. (2023). Knockdown of deleterious miRNA in progenitor cell-derived small extracellular vesicles enhances tissue repair in myocardial infarction. *Sci. Adv.* 9, eabo4616. <https://doi.org/10.1126/sciadv.abo4616>.



93. Jing, R., Scarfo, I., Najia, M.A., Lummertz da Rocha, E., Han, A., Sanborn, M., Bingham, T., Kubaczka, C., Jha, D.K., Falchetti, M., et al. (2022). EZH1 repression generates mature iPSC-derived CAR T cells with enhanced antitumor activity. *Cell Stem Cell* 29, 1181–1196.e6. <https://doi.org/10.1016/j.stem.2022.06.014>.
94. Fortin, A.V., Long, A.S., Williams, A., Meier, M.J., Cox, J., Pinsonnault, C., Yauk, C.L., and White, P.A. (2023). Application of a new approach methodology (NAM)-based strategy for genotoxicity assessment of data-poor compounds. *Front. Toxicol.* 5, 1098432. <https://doi.org/10.3389/ftox.2023.1098432>.
95. Teo, Y.V., Rattanavirotkul, N., Olova, N., Salzano, A., Quintanilla, A., Tarrats, N., Kiourtis, C., Müller, M., Green, A.R., Adams, P.D., et al. (2019). Notch Signaling Mediates Secondary Senescence. *Cell Rep.* 27, 997–1007.e5. <https://doi.org/10.1016/j.celrep.2019.03.104>.
96. Tang, H., Geng, A., Zhang, T., Wang, C., Jiang, Y., and Mao, Z. (2019). Single senescent cell sequencing reveals heterogeneity in senescent cells induced by telomere erosion. *Protein Cell* 10, 370–375. <https://doi.org/10.1007/s13238-018-0591-y>.
97. Eraslan, G., Simon, L.M., Mircea, M., Mueller, N.S., and Theis, F.J. (2019). Single-cell RNA-seq denoising using a deep count autoencoder. *Nat. Commun.* 10, 390. <https://doi.org/10.1038/s41467-018-07931-2>.
98. Saul, D., Kosinsky, R.L., Atkinson, E.J., Doolittle, M.L., Zhang, X., LeBrasseur, N.K., Pignolo, R.J., Robbins, P.D., Niedernhofer, L.J., Ikeno, Y., et al. (2022). A new gene set identifies senescent cells and predicts senescence-associated pathways across tissues. *Nat. Commun.* 13, 4827. <https://doi.org/10.1038/s41467-022-32552-1>.
99. Zhang, X., Habiballa, L., Aversa, Z., Ng, Y.E., Sakamoto, A.E., Englund, D.A., Pearsall, V.M., White, T.A., Robinson, M.M., Rivas, D.A., et al. (2022). Characterization of cellular senescence in aging skeletal muscle. *Nat Aging* 2, 601–615. <https://doi.org/10.1038/s43587-022-00250-8>.
100. Kiselev, V.Y., Yiu, A., and Hemberg, M. (2018). scmap: projection of single-cell RNA-seq data across data sets. *Nat. Methods* 15, 359–362. <https://doi.org/10.1038/nmeth.4644>.
101. Boufe, K., Seth, S., and Batada, N.N. (2020). scID Uses Discriminant Analysis to Identify Transcriptionally Equivalent Cell Types across Single-Cell RNA-Seq Data with Batch Effect. *iScience* 23, 100914. <https://doi.org/10.1016/j.isci.2020.100914>.
102. Duan, B., Zhu, C., Chuai, G., Tang, C., Chen, X., Chen, S., Fu, S., Li, G., and Liu, Q. (2020). Learning for single-cell assignment. *Sci. Adv.* 6, eabd0855. <https://doi.org/10.1126/sciadv.abd0855>.
103. Troiani, M., Colucci, M., D'Ambrosio, M., Guccini, I., Pasquini, E., Varesi, A., Valdata, A., Mosole, S., Revandkar, A., Attanasio, G., et al. (2022). Single-cell transcriptomics identifies Mcl-1 as a target for senolytic therapy in cancer. *Nat. Commun.* 13, 2177. <https://doi.org/10.1038/s41467-022-29824-1>.
104. Chan, M., Yuan, H., Soifer, I., Maile, T.M., Wang, R.Y., Ireland, A., O'Brien, J.J., Goudeau, J., Chan, L.J.G., Vijay, T., et al. (2022). Novel insights from a multiomics dissection of the Hayflick limit. *eLife* 11, e70283. <https://doi.org/10.7554/eLife.70283>.
105. Huang, Q., Wang, Y., Zhang, L., Qian, W., Shen, S., Wang, J., Wu, S., Xu, W., Chen, B., Lin, M., and Wu, J. (2022). Single-cell transcriptomics highlights immunological dysregulations of monocytes in the pathobiology of COPD. *Respir. Res.* 23, 367. <https://doi.org/10.1186/s12931-022-02293-2>.
106. Yao, C., Guan, X., Carraro, G., Parimon, T., Liu, X., Huang, G., Mulay, A., Soukiasian, H.J., David, G., Weigt, S.S., et al. (2021). Senescence of Alveolar Type 2 Cells Drives Progressive Pulmonary Fibrosis. *Am. J. Respir. Crit. Care Med.* 203, 707–717. <https://doi.org/10.1164/rccm.202004-1274OC>.
107. Melms, J.C., Biermann, J., Huang, H., Wang, Y., Nair, A., Tagore, S., Katsyly, I., Rendeiro, A.F., Amin, A.D., Schapiro, D., et al. (2021). A molecular single-cell lung atlas of lethal COVID-19. *Nature* 595, 114–119. <https://doi.org/10.1038/s41586-021-03569-1>.
108. Chou, C.H., Jain, V., Gibson, J., Attarian, D.E., Haraden, C.A., Yohn, C.B., Laberge, R.M., Gregory, S., and Kraus, V.B. (2020). Synovial cell cross-talk with cartilage plays a major role in the pathogenesis of osteoarthritis. *Sci. Rep.* 10, 10868. <https://doi.org/10.1038/s41598-020-67730-y>.
109. Alsaigh, T., Evans, D., Frankel, D., and Torkamani, A. (2022). Decoding the transcriptome of calcified atherosclerotic plaque at single-cell resolution. *Commun. Biol.* 5, 1084. <https://doi.org/10.1038/s42003-022-04056-7>.
110. Solé-Boldo, L., Raddatz, G., Schütz, S., Mallm, J.P., Rippe, K., Lonsdorf, A.S., Rodríguez-Paredes, M., and Lyko, F. (2020). Single-cell transcriptomes of the human skin reveal age-related loss of fibroblast priming. *Commun. Biol.* 3, 188. <https://doi.org/10.1038/s42003-020-0922-4>.
111. Litviňuková, M., Talavera-López, C., Maatz, H., Reichart, D., Worth, C.L., Lindberg, E.L., Kanda, M., Polanski, K., Heinig, M., Lee, M., et al. (2020). Cells of the adult human heart. *Nature* 588, 466–472. <https://doi.org/10.1038/s41586-020-2797-4>.
112. Mao, B., and Niehrs, C. (2003). Kremen2 modulates Dickkopf2 activity during Wnt/IRP6 signaling. *Gene* 302, 179–183. [https://doi.org/10.1016/S0378-1119\(02\)01106-X](https://doi.org/10.1016/S0378-1119(02)01106-X).
113. Wang, G., Lunardi, A., Zhang, J., Chen, Z., Ala, U., Webster, K.A., Tay, Y., Gonzalez-Billalabeitia, E., Egia, A., Shaffer, D.R., et al. (2013). Zbtb7a suppresses prostate cancer through repression of a Sox9-dependent pathway for cellular senescence bypass and tumor invasion. *Nat. Genet.* 45, 739–746. <https://doi.org/10.1038/ng.2654>.
114. Kang, T., Moore, E.C., Kopania, E.E.K., King, C.D., Schilling, B., Campisi, J., Good, J.M., and Brem, R.B. (2023). A natural variation-based screen in mouse cells reveals USF2 as a regulator of the DNA damage response and cellular senescence. *G3 (Bethesda)* 13, jkad091. <https://doi.org/10.1093/g3journal/jkad091>.
115. Lewis, D.A., Travers, J.B., Machado, C., Somani, A.K., and Spandau, D.F. (2011). Reversing the aging stromal phenotype prevents carcinoma initiation. *Aging (Albany, NY)* 3, 407–416. <https://doi.org/10.18632/aging.100318>.
116. Biran, A., Zada, L., Abou Karam, P., Vadai, E., Roitman, L., Ovadya, Y., Porat, Z., and Krizhanovsky, V. (2017). Quantitative identification of senescent cells in aging and disease. *Aging Cell* 16, 661–671. <https://doi.org/10.1111/accel.12592>.
117. Datlinger, P., Rendeiro, A.F., Schmidl, C., Krausgruber, T., Traxler, P., Klughammer, J., Schuster, L.C., Kuchler, A., Alpar, D., and Bock, C. (2017). Pooled CRISPR screening with single-cell transcriptome readout. *Nat. Methods* 14, 297–301. <https://doi.org/10.1038/nmeth.4177>.
118. Hill, A.J., McFaline-Figueroa, J.L., Starita, L.M., Gasperini, M.J., Matreyek, K.A., Packer, J., Jackson, D., Shendure, J., and Trapnell, C. (2018). On the design of CRISPR-based single-cell molecular screens. *Nat. Methods* 15, 271–274. <https://doi.org/10.1038/nmeth.4604>.
119. Dixit, A., Parnas, O., Li, B., Chen, J., Fulco, C.P., Jerby-Arnon, L., Marjanovic, N.D., Dionne, D., Burks, T., Raychowdhury, R., et al. (2016). Perturb-Seq: Dissecting Molecular Circuits with Scalable Single-Cell RNA Profiling of Pooled Genetic Screens. *Cell* 167, 1853–1866.e17. <https://doi.org/10.1016/j.cell.2016.11.038>.
120. Replogle, J.M., Saunders, R.A., Pogson, A.N., Hussmann, J.A., Lenail, A., Guna, A., Mascibroda, L., Wagner, E.J., Adelman, K., Lithwick-Yanai, G., et al. (2022). Mapping information-rich genotype-phenotype landscapes with genome-scale Perturb-seq. *Cell* 185, 2559–2575.e28. <https://doi.org/10.1016/j.cell.2022.05.013>.
121. Huang, J., Liu, Y., Zhang, W., Yu, H., and Han, J.D. (2011). eResponseNet: a package prioritizing candidate disease genes through cellular pathways. *Bioinformatics* 27, 2319–2320. <https://doi.org/10.1093/bioinformatics/btr380>.
122. Drullion, C., Trégoat, C., Lagarde, V., Tan, S., Gioia, R., Priault, M., Djavaheri-Mergny, M., Brisson, A., Auberger, P., Mahon, F.X., and Pasquet, J.M. (2012). Apoptosis and autophagy have opposite roles on imatinib-induced K562 leukemia cell senescence. *Cell Death Dis.* 3, e373. <https://doi.org/10.1038/cddis.2012.111>.
123. Lompardía, S., Díaz, M., Pibuel, M., Papademetrio, D., Poodts, D., Mihalez, C., Álvarez, É., and Hajos, S. (2019). Hyaluronan abrogates

- imatinib-induced senescence in chronic myeloid leukemia cell lines. *Sci. Rep.* 9, 10930. <https://doi.org/10.1038/s41598-019-47248-8>.
124. Acosta, J.C., Banito, A., Wuestefeld, T., Georgilis, A., Janich, P., Morton, J.P., Athineos, D., Kang, T.W., Lasitschka, F., Andriulis, M., et al. (2013). A complex secretory program orchestrated by the inflammasome controls paracrine senescence. *Nat. Cell Biol.* 15, 978–990. <https://doi.org/10.1038/ncb2784>.
125. Acosta, J.C., O’Loghlen, A., Banito, A., Guijarro, M.V., Augert, A., Raguz, S., Fumagalli, M., Da Costa, M., Brown, C., Popov, N., et al. (2008). Chemokine signaling via the CXCR2 receptor reinforces senescence. *Cell* 133, 1006–1018. <https://doi.org/10.1016/j.cell.2008.03.038>.
126. Ortiz-Montero, P., Londoño-Vallejo, A., and Vernot, J.P. (2017). Senescence-associated IL-6 and IL-8 cytokines induce a self- and cross-reinforced senescence/inflammatory milieu strengthening tumorigenic capabilities in the MCF-7 breast cancer cell line. *Cell Commun. Signal.* 15, 17. <https://doi.org/10.1186/s12964-017-0172-3>.
127. Gasek, N.S., Kuchel, G.A., Kirkland, J.L., and Xu, M. (2021). Strategies for targeting senescent cells in human disease. *Nat. Aging* 1, 870–879. <https://doi.org/10.1038/s43587-021-00121-8>.
128. Adler, M., Mayo, A., Zhou, X., Franklin, R.A., Meizlish, M.L., Medzhitov, R., Kallenberger, S.M., and Alon, U. (2020). Principles of Cell Circuits for Tissue Repair and Fibrosis. *iScience* 23, 100841. <https://doi.org/10.1016/j.isci.2020.100841>.
129. Wang, L., Lankhorst, L., and Bernards, R. (2022). Exploiting senescence for the treatment of cancer. *Nat. Rev. Cancer* 22, 340–355. <https://doi.org/10.1038/s41568-022-00450-9>.
130. Guo, H., Xiang, Z., Zhang, Y., and Sun, D. (2019). Inhibiting 6-phosphogluconate dehydrogenase enhances chemotherapy efficacy in cervical cancer via AMPK-independent inhibition of RhoA and Rac1. *Clin. Transl. Oncol.* 21, 404–411. <https://doi.org/10.1007/s12094-018-1937-x>.
131. Lin, R., Elf, S., Shan, C., Kang, H.B., Ji, Q., Zhou, L., Hitosugi, T., Zhang, L., Zhang, S., Seo, J.H., et al. (2015). 6-Phosphogluconate dehydrogenase links oxidative PPP, lipogenesis and tumour growth by inhibiting LKB1-AMPK signalling. *Nat. Cell Biol.* 17, 1484–1496. <https://doi.org/10.1038/ncb3255>.
132. Yang, X., Peng, X., and Huang, J. (2018). Inhibiting 6-phosphogluconate dehydrogenase selectively targets breast cancer through AMPK activation. *Clin. Transl. Oncol.* 20, 1145–1152. <https://doi.org/10.1007/s12094-018-1833-4>.
133. Chen, Y., Lun, A.T., and Smyth, G.K. (2016). From reads to genes to pathways: differential expression analysis of RNA-Seq experiments using Rsubread and the edgeR quasi-likelihood pipeline. *F1000Res* 5, 1438. <https://doi.org/10.12688/f1000research.8987.2>.
134. Yu, G., Wang, L.G., Han, Y., and He, Q.Y. (2012). clusterProfiler: an R package for comparing biological themes among gene clusters. *OMICS* 16, 284–287. <https://doi.org/10.1089/omi.2011.0118>.
135. Efremova, M., Vento-Tormo, M., Teichmann, S.A., and Vento-Tormo, R. (2020). CellPhoneDB: inferring cell–cell communication from combined expression of multi-subunit ligand–receptor complexes. *Nat. Protoc.* 15, 1484–1506. <https://doi.org/10.1038/s41596-020-0292-x>.
136. Angerer, P., Haghverdi, L., Büttner, M., Theis, F.J., Marr, C., and Buettner, F. (2016). destiny: diffusion maps for large-scale single-cell data in R. *Bioinformatics* 32, 1241–1243. <https://doi.org/10.1093/bioinformatics/btv715>.
137. Aibar, S., González-Blas, C.B., Moerman, T., Huynh-Thu, V.A., Imrichova, H., Hulselmans, G., Rambow, F., Marine, J.C., Geurts, P., Aerts, J., et al. (2017). SCENIC: single-cell regulatory network inference and clustering. *Nat. Methods* 14, 1083–1086. <https://doi.org/10.1038/nmeth.4463>.
138. Shannon, P., Markiel, A., Ozier, O., Baliga, N.S., Wang, J.T., Ramage, D., Amin, N., Schwikowski, B., and Ideker, T. (2003). Cytoscape: a software environment for integrated models of biomolecular interaction networks. *Genome Res.* 13, 2498–2504. <https://doi.org/10.1101/gr.1239303>.
139. Liao, Y., Smyth, G.K., and Shi, W. (2014). featureCounts: an efficient general purpose program for assigning sequence reads to genomic features. *Bioinformatics* 30, 923–930. <https://doi.org/10.1093/bioinformatics/btt656>.
140. Kim, D., Paggi, J.M., Park, C., Bennett, C., and Salzberg, S.L. (2019). Graph-based genome alignment and genotyping with HISAT2 and HISAT-genotype. *Nat. Biotechnol.* 37, 907–915. <https://doi.org/10.1038/s41587-019-0201-4>.
141. Pedregosa, F., Varoquaux, G., Gramfort, A., Michel, V., Thirion, B., Grisel, O., Blondel, M., Prettenhofer, P., Weiss, R., Dubourg, V., et al. (2011). Scikit-learn: Machine Learning in Python. *J. Mach. Learn. Res.* 12, 2825–2830.
142. Warren, C.F.A., Wong-Brown, M.W., and Bowden, N.A. (2019). BCL-2 family isoforms in apoptosis and cancer. *Cell Death Dis.* 10, 177. <https://doi.org/10.1038/s41419-019-1407-6>.
143. Youle, R.J., and Strasser, A. (2008). The BCL-2 protein family: opposing activities that mediate cell death. *Nat. Rev. Mol. Cell Biol.* 9, 47–59. <https://doi.org/10.1038/nrm2308>.
144. Ren, X., Zhong, G., Zhang, Q., Zhang, L., Sun, Y., and Zhang, Z. (2020). Reconstruction of cell spatial organization from single-cell RNA sequencing data based on ligand-receptor mediated self-assembly. *Cell Res.* 30, 763–778. <https://doi.org/10.1038/s41422-020-0353-2>.
145. Szklarczyk, D., Gable, A.L., Nastou, K.C., Lyon, D., Kirsch, R., Pyysalo, S., Doncheva, N.T., Legeay, M., Fang, T., Bork, P., et al. (2021). The STRING database in 2021: customizable protein-protein networks, and functional characterization of user-uploaded gene/measurement sets. *Nucleic Acids Res.* 49, D605–D612. <https://doi.org/10.1093/nar/gkaa1074>.
146. Wu, G., Feng, X., and Stein, L. (2010). A human functional protein interaction network and its application to cancer data analysis. *Genome Biol.* 11, R53. <https://doi.org/10.1186/gb-2010-11-5-r53>.



## STAR★METHODS

### KEY RESOURCES TABLE

REAGENT or RESOURCE	SOURCE	IDENTIFIER
<b>Chemicals, Peptides, and Recombinant Proteins</b>		
Bleomycin sulfate	PSAITONG	CAS: 9041-93-4
eosin	HARVEYBIO	CAS:17372-87-1
<b>Critical Commercial Assays</b>		
Senescence-associated $\beta$ -Galactosidase Staining	Beyotime	C0602
Lipofectamine 3000 Transfection Reagent	Thermo Fisher	L3000001
<b>Deposited Data</b>		
Public bulk and single cell RNA-seq data	<a href="#">Table S1</a>	N/A
<b>Experimental Models: Cell Lines</b>		
ARPE-19	ATCC	Cat# CC-Y1051; RRID:CVCL_0145
<b>Oligonucleotides</b>		
Primers for qPCR	<a href="#">Table S6</a>	N/A
siRNA	<a href="#">Table S6</a>	N/A
<b>Software and Algorithms</b>		
SenCID	This paper	<a href="https://github.com/JackieHanLab/SenCID">https://github.com/JackieHanLab/SenCID</a> <a href="https://doi.org/10.5281/zenodo.10693628">https://doi.org/10.5281/zenodo.10693628</a>
Python (version 3.6.13)	Python Software Foundation	<a href="https://www.python.org/">https://www.python.org/</a> ; RRID:SCR_008394
R (version 4.0.3)	R Core Team	<a href="https://www.r-project.org/">https://www.r-project.org/</a> ; RRID:SCR_001905
edgeR (version 3.34.0)	Chen et al. <sup>133</sup>	<a href="https://bioconductor.org/packages/release/bioc/html/edgeR.html">https://bioconductor.org/packages/release/bioc/html/edgeR.html</a> ; RRID:SCR_012802
scikit-learn (version 1.1.1)	N/A	<a href="https://scikit-learn.org/">https://scikit-learn.org/</a> ; RRID:SCR_002577
clusterProfiler (version 3.14.3)	Yu et al. <sup>134</sup>	Version 3.4.4, <a href="https://bioconductor.org/packages/release/bioc/html/clusterProfiler.html">https://bioconductor.org/packages/release/bioc/html/clusterProfiler.html</a> ; RRID:SCR_016884
Seurat (version 4.1.0)	Laboratory of Rahul Satija	<a href="http://satijalab.org/seurat/">http://satijalab.org/seurat/</a> ; RRID:SCR_016341
LandSCENT (version 0.99.5)	Teschendorff and Enver <sup>31</sup>	<a href="https://aeteschendorff-lab.github.io/software/LandSCENT/">https://aeteschendorff-lab.github.io/software/LandSCENT/</a>
CellPhoneDB (version 1.1.0)	Vento-Tormo R, et al. <sup>135</sup>	<a href="https://github.com/ventolab/CellphoneDB">https://github.com/ventolab/CellphoneDB</a> ; RRID:SCR_017054
destiny (version 3.1.1)	Angerer et al. <sup>136</sup>	<a href="https://bioconductor.org/packages/release/bioc/html/destiny.html">https://bioconductor.org/packages/release/bioc/html/destiny.html</a>
gam (version 1.20.1)	N/A	<a href="https://CRAN.R-project.org/package=gam">https://CRAN.R-project.org/package=gam</a>
pySCENIC (version 0.10.3)	Aibar, A. et al. <sup>137</sup>	<a href="https://pyscenic.readthedocs.io/en/latest/index.html">https://pyscenic.readthedocs.io/en/latest/index.html</a>
pheatmap (version 1.0.12)	N/A	<a href="https://github.com/raivokolde/pheatmap">https://github.com/raivokolde/pheatmap</a> , RRID:SCR_016418
ImageJ	NIH	<a href="https://imagej.nih.gov/ij/">https://imagej.nih.gov/ij/</a> ; RRID:SCR_003070
Adobe Illustrator CC	Adobe Systems	<a href="https://www.adobe.com/products/illustrator.html">https://www.adobe.com/products/illustrator.html</a> ; RRID:SCR_010279
Cytoscape (version 3.8.2)	Shannon et al. <sup>138</sup>	<a href="https://cytoscape.org/">https://cytoscape.org/</a> ; RRID:SCR_015784
Trim galore	Babraham Institute	<a href="https://github.com/FelixKrueger/TrimGalore">https://github.com/FelixKrueger/TrimGalore</a> ; RRID:SCR_011847
FeatureCounts (version 2.0.1)	Liao et al. <sup>139</sup>	<a href="https://subread.sourceforge.net/featureCounts.html">https://subread.sourceforge.net/featureCounts.html</a> ; RRID:SCR_012919
Samtools (version 1.14)	N/A	<a href="http://samtools.sourceforge.net/">http://samtools.sourceforge.net/</a> , RRID:SCR_002105
HISAT2 (version 2.1.0)	Kim et al. <sup>33</sup>	<a href="https://daehwankimlab.github.io/hisat2/manual/">https://daehwankimlab.github.io/hisat2/manual/</a> ; RRID:SCR_015530

## RESOURCE AVAILABILITY

### Lead contact

Further information and requests for reagents should be directed and will be fulfilled by the lead contact (Jing-Dong J. Han, [jackie.han@pku.edu.cn](mailto:jackie.han@pku.edu.cn)).

### Materials availability

The study did not generate new unique reagents.

### Data and code availability

- All datasets used in this study are already published and are obtained from public data repositories, including GEO (<https://www.ncbi.nlm.nih.gov/geo/>) and EBI (<https://www.ebi.ac.uk>). See Table S1 for detailed information, where the accession number, cell type information, etc. of every sample is listed. All other relevant data supporting the key findings of this study are available within the article or the [supplemental information](#) files. Source data are provided with this paper (Data S1).
- The package is available at Github: <https://github.com/JackieHanLab/SenCID> and Zenodo: <https://doi.org/10.5281/zenodo.10693628>.
- Any additional information required to reanalyze the data reported in this paper is available from the [lead contact](#) upon request.

## EXPERIMENTAL MODELS

### Cell culture and treatment

ARPE-19 (retinal pigment epithelia cell line derived from the normal eyes of a 19-year-old male) was grown in RPMI-1640 supplemented with 10% fetal bovine serum (FBS) and 1% penicillin-streptomycin. Cells were maintained at 37°C with 5% CO<sub>2</sub>. The treatment of bleomycin (20 µg/mL) was performed after 24 hours of transfection with siRNA, and the treatment takes another 24 hours.

## METHOD DETAILS

### siRNA transfection

Cells were grown to ~50% confluence and then transfected with siRNA using Lipofectamine 3000 Transfection Reagent (Thermo Fisher) according to the manufacturer's protocol. Cells transfected with non-specific, scrambled siRNA (Life Technologies) served as a negative control. Follow-up experiments are applied 96 hours after transfection, and the transfection process was repeated every 48 hours after the first-time transfection to keep the knock-down efficiency. The efficiency was assessed by Real-time quantitative PCR (RT-qPCR). Total RNA was isolated using TRIzol reagent, followed by reverse transcription into cDNA using the PrimeScript RT reagent Kit with gDNA Eraser (Takara, Japan). qPCR was performed using TB Green Premix (Takara, Japan). The target mRNA expression levels were analyzed using the  $\Delta\Delta C_t$  method and normalized to expression levels of GAPDH, used as an internal control. The sequence of siRNA and primers for RT-qPCR are listed in Table S6.

### Senescence-associated $\beta$ -galactosidase staining and quantitation

The ARPE-19 cells were fixed and stained with a senescence-associated  $\beta$ -Galactosidase Staining Kit (Beyotime, China) according to the manufacturer's instructions. Staining was performed overnight at 37°C in darkness with the working solution containing 0.05 mg/mL 5-bromo-4-chloro-3-indolyl- $\beta$ -galactopyranoside (X-gal). The cells were washed with PBS for 2 times the following day, dyed with eosin solution for 30s, and were observed under a microscope after washing with ethanol for 2 times. The senescence levels were represented by the ratio of SA- $\beta$ -gal-positive area in eosin-positive area detected by the program ImageJ. Average values from five to six images were taken for each well of cells, and 3 replicate wells were in each condition for comparison.

### Data collection and pre-processing

Transcriptome data of both bulk and single cell RNA-seq are collected from public data repositories. To ensure high-quality data, only cell types with both senescent and non-senescent samples confirmed by at least two experimental proofs are included in BTD. One proof must be either SA- $\beta$ -gal staining (if the SA- $\beta$ -gal positive ratio is quantified, only samples with positive ratios > 40% are taken as senescent and < 20% as non-senescent as claimed by the original studies) or growth curve analysis. The sample information is summarized in Table S1.

For each dataset, we collect the raw count matrix. If the count matrix is not available publicly, we use HISAT2<sup>140</sup> (v2.1.0) for alignment to the GRCh38 human genome and featureCounts (v2.0.1)<sup>139</sup> for genome annotation on gencode.v35 database.

To construct the senescence-related candidate gene set, we combine five datasets: SeneQuest,<sup>7</sup> CSGene,<sup>24</sup> CellAge,<sup>22</sup> CellSig,<sup>23</sup> and SASP genes from De Cecco et al.<sup>59</sup> We exclude genes that expressed less than 1 count in over 60% of each

batch. We normalize the  $\log_2(\text{count per million} + 1)$  value for each gene in the final gene set (1,290 SRGs) by z-score for each sample or cell.

### Machine learning and non-machine learning-based senescence estimator

The 3 types of machine learning-based classifier we test, SVM, RandomForest, and MLPC, are all built using scikit-learn (v0.24.2) python package,<sup>141</sup> and hyper-parameter search is conducted using grid search. We also perform GSVA-based and Seurat AddModuleScore-based senescence estimations using R packages GSVA (v1.40.1), escape (v1.3.4) and Seurat (v4.1.0), using features and parameters recommended by the previous publications.<sup>25,26</sup> To compare the performance of these methods, we perform leave-one-cell-type-out strategy for all methods, which splits the dataset into separate train and test sets according to cell types, each time use one cell type as test set while the others as training set. Only predictions of test sets are used for evaluation of model performance. We use the area under the receiver operating characteristic (ROC) curve (AUC) as a metric. The decision function or probabilities given by the algorithms are used to calculate the AUC, and the R package pROC (v1.18.0) is used for this analysis.

### SenCID package construction

The feature-selection and model-training for senescence classification are performed using the Support Vector Machine–Recursive Feature Elimination (SVM-RFE) module in the scikit-learn python package<sup>141</sup> (v0.24.2). Multiple SVM-RFE models are constructed, each trained on one cell type with both senescent and non-senescent samples >10, while other cell types are used for validation. For lung fibroblast with abundant samples, we randomly sample half of the samples (83 samples from 6 batches) for training and the other half (85 samples from independent 8 batches) is combined to form the validation set.

Five-fold cross-validation is used for the training samples, and a step-length of 1 is used in RFE to eliminate features until no feature is left. The optimal number of features ( $i_{\text{opt}}$ ) is defined as the number where the AUC-feature number curves of 5-cv training set and validation set both reach the elbow point (Figure S2D). Then, the performance of the resulting SVM model with  $i_{\text{opt}}$  features is evaluated on each cell type other than the training set, and cell types with an accuracy over 0.95 are classified into the same SID as the training set. Coefficients of feature genes on each SID model are obtained from the '.coef\_' attribute of the sklearn package. To obtain a normalized senescence probability ranging from 0 to 1, a logistic regression model is built using the selected features from each RFE-SVM SID model, and the resulting output is denoted as the SID Score. The SID Score is highly correlated with the decision function result from SVM (Figure S2B, Spearman Correlation > 0.98 in all 6 SIDs). If any cell types remain unclassified, different combinations of two cell types are used for training to obtain the final two SIDs (SID2 and SID6). The process is illustrated in Figure S2A and can be described by the following pseudo code:

Input: RNA-seq data X of total cell types C with the corresponding senescence-or-not labels Y

for one cell type  $C_t$ :

$X_{\text{train}}, Y_{\text{train}} = (X, Y) \mid \text{celltype} == C_t$

$X_{\text{val}}, Y_{\text{val}} = (X, Y) \mid \text{celltype} \neq C_t$

$\{\text{model}\}_i = \text{RFE}(\text{SVM}, \text{FeatureNumber} = i).train(X_{\text{train}}, Y_{\text{train}})$

$\{Y_{\text{train}}^{\text{cv}}\}_i = \text{CrossValidation}(\{\text{model}\}_i)$

$\{Y_{\text{val}}^{\text{pred}}\}_i = \{\text{model}\}_i.predict(X_{\text{val}})$

$i_{\text{opt}} = \min(\text{which.i}(\text{AUC}(Y_{\text{train}}, \{Y_{\text{train}}^{\text{cv}}\}_i) \text{ saturated}))$

&  $\text{which.i}(\text{AUC}(Y_{\text{val}}, \{Y_{\text{val}}^{\text{pred}}\}_i) \text{ saturated}))$

for other cell types  $C_k \neq C_t$ :

$\{Y_{\text{model}}^{C_t}\}_{C_k} = \{\text{model}\}_{i_{\text{opt}}}.predict(X[\text{celltype} == C_k])$

if  $\exists (C_k \subseteq C): \text{Accuracy}(Y_{C_k}, \{Y_{\text{model}}^{C_t}\}_{C_k}) > 0.95$ ,

new SID model =  $\{\text{model}\}_{i_{\text{opt}}}$

new SID celltype group =  $\{\text{all } C_k\}$

SID model features =  $\{\text{model}\}_{i_{\text{opt}}}.features$

SID Score =  $\text{LogisticRegression}(\text{features} = \text{SID model features})$

.train( $X_{\text{train}}$ ).probability

else next

The Recommend function in SenCID is used to suggest the most appropriate SID for a given cell or sample. The function employs a multi-class SVM model trained by the BTM with hyper-parameters selected through grid search ('C': 0.01, 'kernel': 'linear'). Both senescent and non-senescent samples are used to train the model, and its accuracy is evaluated by 10-fold cross-validation. For every cell or sample in the query data, six recommendation indices defined by the decision function output from the one-versus-rest multi-class SVM model, which represents the distance between each sample to the hyperplane of supporting vector. The SID with the highest recommendation index is considered to be the classification of the sample.

For single cell data, DCA imputation<sup>97</sup> is performed prior to normalization and scaling using the dca (v0.3.4) Python package. The SID of a cell type in the scRNA-seq data is the SID with the highest mean recommendation indices of all cells in that cell type.

### RNA-seq data analysis and gene set enrichment

For the analysis of differential gene expression, we utilize the R package edgeR (v3.34.0)<sup>133</sup> for normalization and DEG calling. Genes with a count per million (cpm) of less than 1 in over 90% of the samples within each batch are excluded.

To identify DEGs between different SIDs, only non-senescent samples (a total of 287) are used. The ExactTest function in edgeR is used to compare samples from each SID with all others. PCA-clustering is then performed on the DEGs with the top 100 log<sub>2</sub> fold changes, and gene clusters that specifically highly-expressed in certain samples instead of the whole SID are regarded as bias and outliers and are excluded from the SID marker set.

To perform PCA-clustering, we first normalize the log<sub>2</sub> cpm data by z-scoring first among genes and then among samples. We then utilize the scikit-learn python package (v1.1.1) to perform PCA reduction on the samples/genes and k-means clustering on the genes/samples. The optimal number of principal components and clusters is determined by finding the elbow point on the number of components versus explained variance ratio plot.

To identify senescent markers in each SID, we perform differential gene expression analysis using the exactTest function in edgeR, comparing senescent versus non-senescent samples within each SID. The resulting DEG list is subjected to Gene Set Enrichment Analysis (GSEA) on Gene Ontology (GO) terms using the GSEA function in the R package clusterProfiler (v3.14.3)<sup>134</sup> with default parameters. Enrichment is considered significant for terms with  $p < 0.05$  and Normalized Enrichment Score (NES)  $> 0$ . Genes with BH-corrected  $p < 0.05$  and log<sub>2</sub> fold change (logFC)  $> 1$  are designated as SID-ups, while those with BH-corrected  $p < 0.05$  and logFC  $< -1$  are designated as SID-downs.

To compare the inflammation, ribosomal protein and anti-apoptotic levels among SIDs and senescence states, single-sample gene set scores are calculated using the function GSVA in R package GSVA. For the inflammation levels, the gene set is from the term 'HALLMARK\_INFLAMMATORY\_RESPONSE' from MsigDB. For ribosomal protein levels, we use all genes begin with 'RPL' or 'RPS'. For anti-apoptotic BCL2 family proteins, we use the proteins reported in the reviews<sup>142,143</sup> as the gene set. G1/S, G2/M, and M/G1 (spindle and metaphase-to-anaphase) checkpoint-related genes are collected from GO.

Entropy estimation is performed using CompSRana function in LandSCENT R package (v.0.99.5). Data matrix is normalized by log<sub>2</sub>(cpm + 1.1). The function DolntegPPI is used to compute the correlations with the connectome and transcriptome based on the 'net17Jan16.m' PPIs.

### Single cell analysis

Data normalization, batch correction, clustering and visualization of single cell datasets are all done by R package Seurat (v4.1.0). Annotations of cell types are done manually based on reported markers. The DEGs between groups are calculated by function FindMarkers with default parameters, except that logfc cutoff is set to 0 for GSEA analysis.

For the existing methods that are benchmarked against, default parameters are used as provided by the respective studies. Gene set scores are calculated by AddModuleScore function from Seurat R package (v4.1.0). The gene set of Teo et al. comprises the top 300 DEGs between the senescent and non-senescent cells identified in their paper. For the cluster sampling tools like ScMap, ScID and scLearn, BTD is given as the reference data annotated with senescent and non-senescent states to fairly compare only the computational algorithms. For some tools that only output the similarity of a cell with its most probable prediction (senescence or non-senescence), negative similarities are considered as non-senescent prediction probability, while positive similarities are used as senescent prediction probability, enabling the computation of area under the curve (AUC) scores.

The cell-cell communication analysis is done using CellPhoneDB<sup>135</sup> (v1.1.0), with the default reference database along with the ligand-receptor database in Ren et al.'s study.<sup>144</sup> The average expression of each ligand-receptor pair is compared between the most senescent (with the top 25% SID Score) and the least senescent (with the bottom 25% SID Score) cells, and only pairs with  $p < 0.05$  and top 50 |Log2(FoldChange)| are used for visualization by circo plot generated by R package circlize. An autocrine interaction of senescence is identified when both the ligand and receptor of the interaction is expressed in the senescent cell group (Cell\_q4).

To analyze the trajectory of senescence, we utilize the diffusion map algorithm with R package destiny (v3.1.1).<sup>136</sup> We utilize the senescence-related genes, which are the differentially expressed genes (DEGs) between senescent and non-senescent samples within each SID with BH-corrected  $p < 0.05$  and |logFC|  $> 1$ , as variables to build the trajectory. Cells are randomly sampled to the same cell numbers between each pathological condition (1000 for each condition if  $> 1000$  cells, otherwise the smallest hundreds), and the diffusion component (DC) with the highest variance of SID Scores (usually DC1) is defined as the senescence-related DC. Cells are then sorted by their projection on that component.

To identify gene expression changes along the senescence trajectory, we fit generalized additive models using the gam function in the R package gam (v1.20.1) on the expressions of the top 2000 highly variable genes with the senescence DC. The up-regulated, intermediate and down-regulated gene groups are clustered and visualized by R package pheatmap (v1.0.12). For up- and down-regulated genes, only consider those with significant Anova for parametric effects (BH-corrected  $p < 0.05$ ); and for intermediate genes, only consider those with significant Anova for non-parametric effects (BH-corrected  $p < 0.05$ ). The enrichGO in R package clusterProfiler is used to obtain gene function enrichment.

Regulatory network analysis is performed using pySCENIC (v0.10.3).<sup>137</sup> To evaluate the dynamics of TF regulons along the senescent trajectory, the regulon activities from AUCell are fitted in generalized additive models (gam (v1.20.1)) with the senescent DC. The clustering methods and cutoffs for up-regulated, intermediate and down-regulated regulons are the same as described above for trajectory-associated genes.

To estimate the binarization threshold, up-regulated genes are derived from the above trajectory analysis. The elbow point is determined from their mean expression curve of gam-smoothed gene expression along the trajectories. In detail, each point on the mean expression curve is calculated with a distance from the straight line linking the first and last point of the curve, and the point with the longest distance is determined as the elbow point. The corresponding binarization threshold is established by the median SID Scores from 2.5% of the total trajectory cell number around the elbow point (e.g., from 10 cells before to 10 cells after the elbow point in a trajectory containing 800 cells).

For CROP-seq and perturb-seq data, genetic perturbation information is obtained from the original metadata. Perturbed cells are defined as those with sgRNA barcodes targeting a specific gene, while non-perturbed cells have non-targeting control sgRNAs. For Perturb-seq in K562, we exclude cells that still express 1/4 or more of the perturbed gene compared to non-targeted cells to filter out low-quality cells and enrich perturbation-induced senescent cells. Senescence-promoting perturbations are defined as those with perturbed cells having significantly higher SID Score and a greater than 3-fold increase in senescent cell (SID Score > 0.5) ratio compared to non-targeted cells (BH-corrected Wilcoxon test  $p < 0.05$ ). As K562 non-perturbed cells have no senescent cells, perturbations having significantly higher SID Score and at least one cell with SID Score > 0.5 are considered senescence-promoting perturbations. Senescence-suppressing perturbations are defined as those with perturbed cells having significantly lower SID Score compared to non-targeted cells (BH-corrected Wilcoxon test  $p < 0.05$ ). For each senescence-promoting or senescence-suppressing perturbation, Seurat's FindMarkers function is used to identify DEGs compared to non-targeted cells. The fold changes of all genes except those not significantly changed by any perturbation (BH-corrected  $p > 0.05$ ) are used for embedding and clustering of perturbations. Loading on the major PCA components of the fold changes are used for tSNE embedding using R package Rtsne (v0.16), with the number of PCs decided by the elbow point on the number of components versus explained variance ratio plot. Hierarchical clustering is performed using ward.D agglomeration method on the tSNE results, followed by manual combination of clusters with similar GO-term functions. The fold change of each perturbation group is used as the rank list for GSEA analysis.

### eResponseNet network analysis

The eResponseNet package<sup>121</sup> is used to identify molecular pathways responsible for inducing senescence signatures. We consider the perturbation target genes as input source genes and the top 200 and bottom 200 DEGs after each perturbation as input effect genes. We combine STRING database<sup>145</sup> (confidence scores > 600) and the human functional protein interaction network constructed by Wu et al.<sup>146</sup> as a network template, where edges are weighted by the Pearson correlation between pseudobulk z-normalized gene expression profiles. To determine the optimal gamma value, we scan parameter gamma from 3 to 10 and identify the elbow point of eResponseNet edge numbers. The visualization of the network is performed by Cytoscape (v3.8.2).<sup>138</sup> We collect genes associated with G1/S, G2/M, and M/G1 (spindle and metaphase-to-anaphase) checkpoints from GO and examine their enrichment significance in each network using Fisher's exact test (BH-corrected  $p < 0.05$ ).

### QUANTIFICATION AND STATISTICAL ANALYSIS

Statistical analyses are performed with R version 4.0.3, using two-tailed Student's t-tests or Wilcoxon tests as appropriate. Spearman rank-correlation coefficient is used to measure the correlations. All of the statistical tests performed are indicated in the figure legends. The data are presented as mean or individual points with box plots that display the median and quartiles. Error bars represent standard error or 95% confidence interval around the mean, as specified in the figure legends.